Reviews in Mineralogy & Geochemistry
Vol. 61, pp. 127-180, 2006

Electrical and Magnetic Properties of Sulfides

Carolyn I. Pearce, Richard A.D. Pattrick, David J. Vaughan

School of Earth, Atmospheric and Environmental Sciences, and Williamson Research Centre for Molecular Environmental Science
University of Manchester
Manchester, United Kingdom
e-mail: carolyn.pearce@manchester.ac.uk

INTRODUCTION

The metal sulfides exhibit a great diversity of electrical and magnetic properties with both scientific interest and practical applications. These properties apply major constraints on models of the electronic structure (or chemical bonding) in sulfides (Vaughan and Rosso 2006, this volume). The pure and doped synthetic equivalents of certain sulfide minerals have actual or potential applications in the electronics industries (optical devices, photovoltaics, photodiodes and magnetic recording devices). Sulfides are also components of many thin film devices and have been extensively investigated as part of the nanotechnology revolution. Certain electrical and magnetic properties of sulfide minerals mean they contribute to geomagnetism and paleomagnetism, and provide the geophysical prospector with exploration tools for metalliferous ore deposits. To the mineral technologist, these same properties provide methods for the separation of the metal-bearing sulfides from associated waste minerals after mining and milling and before extraction of the metal by pyrometallurgical or hydrometallurgical treatment.

In this chapter, the theory and measurement of electrical and magnetic properties are outlined along with spectroscopic and diffraction studies that can provide insights into magnetic behavior are discussed. A brief review of electrical and magnetic studies of major sulfide minerals includes some examples of the applications of sulfide electrical and magnetic properties, including special consideration of the properties of sulfide nanoparticles. Most of the available data presented are for pure synthetic binary and ternary sulfides, as very small concentrations of impurities can dramatically affect electrical properties leading to problems of interpreting data from natural samples. Although data for several of the commonly found sulfides are discussed in this chapter, no attempt is made at a comprehensive coverage.

The section below on theory and measurement of electrical and magnetic properties draws on the account given in Vaughan and Craig (1978) to which readers are referred for further details. It is useful to provide this overview as the electrical and magnetic properties of sulfides provide critically important information for understanding them as materials, as well as giving rise to important applications. Also, the theoretical background is not commonly dealt with in texts concerning mineralogy or geochemistry, hence its inclusion here.

THEORY AND MEASUREMENT OF ELECTRICAL AND MAGNETIC PROPERTIES

Electrical properties

Metals, in which characteristically high conductivity is associated with overlapping valence and conduction bands or a partly filled band (see below and Vaughan and Rosso 2006),

1529-6466/06/0061-0003$010.00 DOI: 10.2138/rmg.2006.61.3

have room-temperature conductivities which are largely independent of impurities or lattice defects. Generally, the electrical conductivity (σ) is given by the expression:

$$\sigma = \frac{Ne^2\tau}{m} \quad (1)$$

where N = concentration of "free" (conduction) electrons, e = electron charge (1.6×10^{-19} coulombs), m = electron mass, and τ = relaxation time (approximate mean time between collisions for the electron) This generalized expression derives from the "free-electron model" for metals. It shows that conductivity is mainly influenced by the number of conduction electrons (i.e., position of the metal in the periodic table) and the mean time between collisions which scatter the electrons. The lattice vibrations causing the scattering clearly dominate at room temperature but would be expected to die out (i.e., τ would go to infinity) at 0 K and the conductivity becomes infinite in a perfect crystal. Since no real crystal is perfect, resistivity does not fall to zero and, at lower temperatures, impurities and defects have a marked effect. By contrast, the resistivity of metals at relatively high temperatures varies only slowly with temperature. The quantity $e\tau/m$ is defined as the mobility (μ) and is the drift velocity per unit electric field. The "free-electron model" from which these expressions are derived is a classical model which does not involve quantum mechanics and, although adequate in describing conductivity, breaks down when applied to other properties such as magnetic susceptibility.

Semiconductors characteristically exhibit conductivity which increases rapidly as a function of temperature over certain ranges. In the pure intrinsic semiconductor a filled valence band is separated by a narrow energy gap from the vacant conduction band, although this situation is only really applicable at 0 K. As the temperature is raised, the Fermi surface becomes "fuzzy" and electrons are excited above this level by thermal energies of amount kT,[†] and as more and more of them receive enough energy to cross the forbidden gap and become effectively "free," the conductivity increases. Impurities which act as donors or acceptors of electrons complicate the situation by having electronic energies that fall in the forbidden energy gap. The donor levels provide electrons for the conduction band and such (negative) electron conduction is called *n*-type, whereas in *p*-type conduction, the excitation of electrons from the valence band into acceptor levels results in (positive) holes in the valence band. Both are examples of extrinsic semiconduction and both may occur in the same sample. If so, donor levels may empty into acceptor levels and when equal in concentration, effectively compensate for each other. Since intrinsic and extrinsic semiconduction are both temperature-dependent properties, many real examples exhibit temperature ranges over which either intrinsic or extrinsic mechanisms dominate. The concentrations of holes and of electrons in both the intrinsic and extrinsic ranges can be treated as problems in establishing chemical equilibria.

It is important to emphasize that occupation of energy states by electrons in the valence band and conduction band of semiconductors is statistical, and dependent on the number of available states and on the absolute temperature. In an intrinsic semiconductor, it can be shown that above 0 K, the probability factor is one half of the energy between occupied and empty states. This defines the Fermi energy (E_F) and the position of the Fermi level, see Figures 1a and 1b. This is also the activation energy (E_a) required for electrical conduction, which in this simple case is half the energy of the forbidden (or band) gap (i.e., $E_a = ½\ E_g$).

Measurement of electrical properties

A wide range of techniques is available for the measurement of the electrical properties of materials, but only a small number need be considered here. The main properties of interest to

[†] Boltzmann's constant, K, is given by R/N_A where R is the gas constant and N_A is Avogadro's number. It has the value of 1.380×10^{-16} erg K^{-1}.

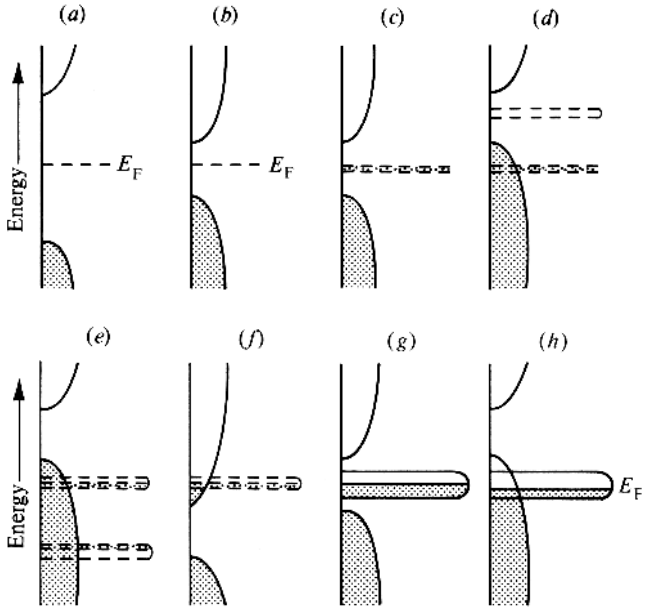

Figure 1. Simplified band models for main group sulfides (at 0 K). Energy (E) is plotted versus the density of states (i.e., statistical occupancy of the energy levels). Occupied states are shaded and empty states are open; localized d levels are shown with broken lines. (a) main group element insulator with wide energy gap (E_F = Fermi level); (b) Main group element semi-conductor (intrinsic); (c) and (d) transition element semiconductors with paramagnetism or diamagnetism; (e) and (f) transition element metallic conductors (p- and n-type respectively) with paramagnetism; (g) and (h) transition metal conductors with Pauli paramagnetism. After Jellinek (1972).

the sulfide mineralogist are those which characterize the material as a metal or semiconductor, give the band gap for the latter, and provide information on conduction mechanisms. As shown above for metals, conductivity is a function both of carrier (electrons or holes) concentration and carrier mobility; unfortunately, more than just conductivity must be known to determine these.

Values of conductivity (or its reciprocal, resistivity) range over about 25 orders of magnitude for all known compounds. Ranges of resistivity for a number of natural sulfide minerals are given in Table 1 and plots of resistivity against reciprocal temperature in Figure 2. Resistivity is normally measured in terms of resistance, which is a function of sample geometry, so that careful orientation and measurement of samples is required, although single crystals are not necessary in many cases because it is possible to achieve good electrical connectivity in polycrystalline materials. Conductivity relates to the current density and the electric field:

$$J = \sigma E \tag{2}$$

where J = current density in amperes cm^{-2}, σ = conductivity in Ω^{-1} cm^{-1}; and E = electrical field in V cm^{-1}. The current density (J) for a hole charge-carrier system is given by:

$$J = p\ eV_\alpha \tag{3}$$

where p = number of hole carriers per cm^3, e = electronic charge (1.6×10^{-19} coulombs), V_α = average velocity of carriers in cm s^{-1}. When Equation (3) is combined with Equation (2):

$$\sigma = pe\frac{V_\alpha}{E} \tag{4}$$

Table 1. Electrical resistivity of certain sulfide ores and minerals. After Parasnis (1956).

Mineral	Formula	Resitivity (ohm cm)	
		Ore	**Mineral**
Pyrite	(FeS_2)	0.01-1000	0.005-5
Chalcopyrite	($CuFeS_2$)	0.01-10	0.01-0.07
Pyrrhotite	($Fe_{1-x}S$)	0.001-0.1	0.001-0.005
Arsenopyrite	(FeAsS)	0.1-10	0.03
Löllingite	($FeAs_2$)	—	0.003
Cobaltite	(CoAsS)	—	1-5
Galena	(PbS)	1-30000	0.003-0.03

This is often written:

$$\sigma = pe\mu_p \tag{5}$$

where μ_p is the carrier mobility of holes in $cm^2\ V^{-1}\ s^{-1}$. This equation shows the dependence of conductivity on both carrier concentration and mobility. A similar equation applies to electrons as charge carriers, and where both are involved then:

$$\sigma = e(\mu_n n + \mu_p p) \tag{6}$$

where n and p are the electron and hole concentrations and μ_n, μ_p their respective mobilities. Techniques for conductivity measurement are described by van der Pauw (1958), Fischer et al. (1961), and Baleshta and Keys (1968).

Hall effect measurements are a method of determining the mobility of charge carriers. The Hall effect is observed when a magnetic field is applied at right-angles to a conductor carrying a current (Fig. 3). The magnetic field deflects the current carriers and a restoring force (the Hall potential) is generated in order to maintain equilibrium so the current can continue flowing. This equilibrium can be expressed as:

$$B\,eV = eE_H \tag{7}$$

where B = magnetic flux density in gauss, e = electronic charge (1.6×10^{-19} coulombs), V = velocity of the carriers in cm s^{-1}, E_H = Hall field in v cm^{-1}. The average velocity of the charge carriers can be expressed in terms of the current density (J) and the conduction electron density (n), since $J = n\,eV$. Then, substituting in Equation (7) gives:

$$E_H = \left(\frac{I}{ne}\right)JB = RJB \tag{8}$$

where R = the Hall constant = I/ne, which gives the carrier concentration directly. What is experimentally determined is the Hall voltage (V_H), which is the potential actually measured across the sample in the direction normal to the current and magnetic field directions. It is dependent on sample geometry ($E_H = V_H/w$ where w = sample width; also $J = I/wt$ where I = current flowing through sample, t = sample thickness). Thus Equation (8) becomes:

$$R = \frac{I}{ne} = \frac{V_H t}{1B} \tag{9}$$

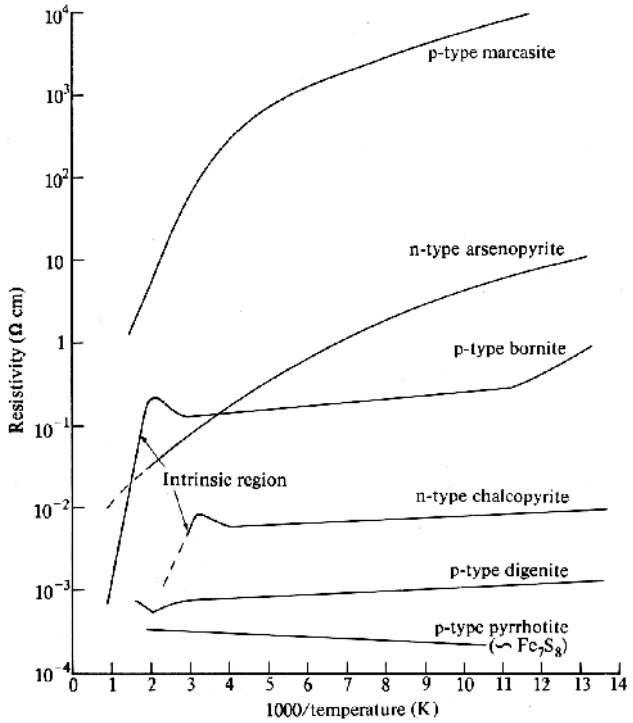

Figure 2. Resistivity versus reciprocal temperature for several sulfides. Modified after Baleshta and Dibbs (1969).

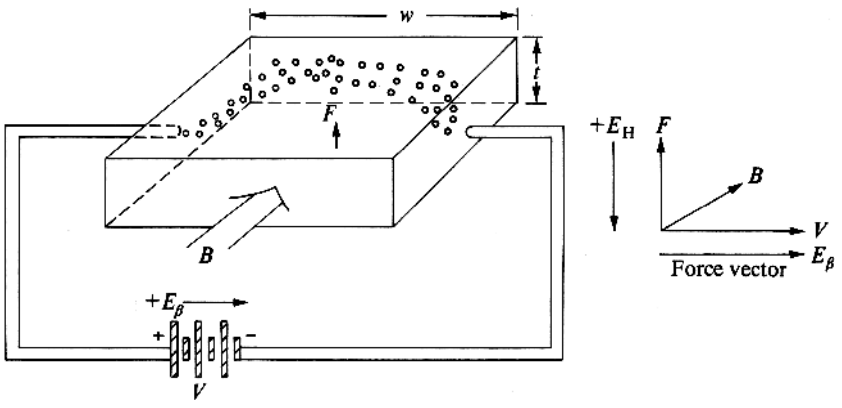

Figure 3. The Hall effect experiment – the effect of a magnetic field on positive charge-carriers in a crystal.

and the carrier concentration is given from the measured Hall voltage and known applied current and magnetic field. The sign of the Hall voltage indicates whether the carriers are holes $^{(+)}$ or electrons $^{(-)}$. As shown in Equation (5), carrier mobility is a function of electron or hole concentration (expressed as n and p respectively) and conductivity. Thus, from combined Hall effect and conductivity measurements, the mobility of electron (μ_n) or hole (μ_p) carriers may be determined; that is:

$$\mu_n = R\sigma \text{ for electrons (where } R = I/ne) \\ \mu_p = R\sigma \text{ for holes (where } R = I/pe) \tag{10}$$

This applies to cases where the conduction is overwhelmingly due to either electrons or holes. Where both electrons and holes play an important role, as in intrinsic semiconductors:

$$R = \frac{p - nb^2}{(p + nb)^2 e} \tag{11}$$

Where $b = \mu_n/\mu_p$. It is possible for the sign of the Hall voltage to change with temperature in such samples. The relationship between n and p shown in Equation (11) has to be established by further experiments involving varying the sample composition and temperature of measurement. Data for mobility as a function of temperature in some galena and pyrite samples are shown in Figure 4.

Thermoelectic power measurements show the tendency of mobile charge carriers to move from the hot end to the cold end of a sample which is placed in a temperature

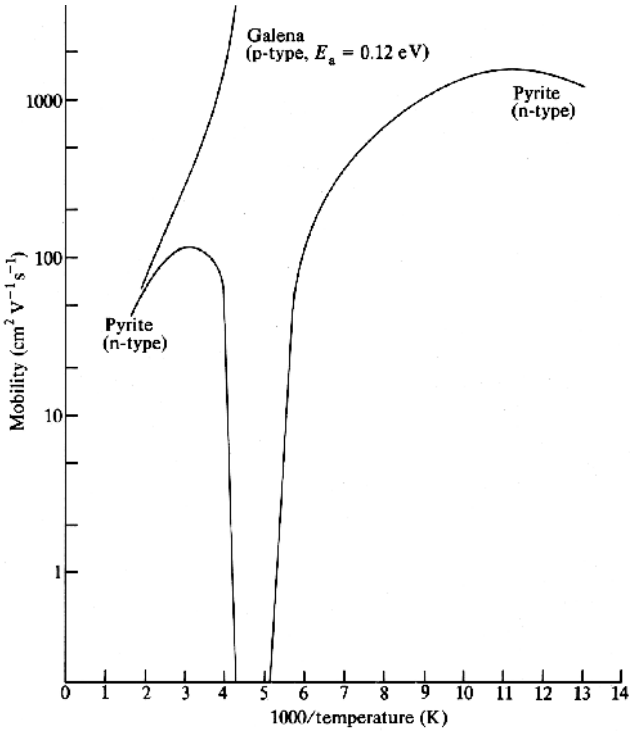

Figure 4. Mobility versus reciprocal temperature for a galena sample (hole mobility) and an *n*-type pyrite (electron mobility). Modified after Baleshta and Dibbs (1969).

gradient. Thus, if two contacts are placed on areas of the sample maintained at different temperatures, the potential difference measured between them is called the Seebeck voltage (normally expressed as V deg K^{-1}). The polarity of this thermoelectric voltage can be used to determine the sign of the majority carrier in a semiconductor, since electrons give rise to negative Seebeck voltages, whereas hole carriers result in a positive potential. The variation of thermoelectric power with temperature gives information regarding the activation energy and the position of the Fermi level:

$$\Phi_T = -\frac{k}{e}\left[A - \frac{(E_c - E_F)}{kT}\right] \tag{12}$$

Where Φ_T = thermoelectric power (V K^{-1}) at temperature T (K), K = Boltzmann constant, e = electronic charge, A = constant (≈2), E_c = energy of bottom of conduction band, E_F = Fermi energy. The Seebeck coefficients measured for pyrite-type disulfides, for example, range from −500 to +311 and can be correlated with conduction mechanism (Table 2). Plots of Φ_T against temperature are shown for several sulfides in Figure 5.

Magnetic properties

All materials can be categorized into a number of general classes according to their response to magnetic fields. When a magnetization is induced which opposes the external magnetic field, the material is diamagnetic. When the induced magnetization is parallel to the external field, the material is paramagnetic. Paramagnetism results from the presence of atoms with permanent magnetic dipoles, and commonly occurs in atoms or molecules with unpaired electrons. This is because a single electron can be regarded, in terms of a classical model, as a magnet formed by the spinning of the negatively charged particle on its axis. Also, an electron traveling in a closed path around the nucleus produces a magnetic moment. The magnetic moments of atoms, ions and molecules are expressed as Bohr magnetons (BM or μ_B):

$$1\mu_B = \frac{eh}{4\pi mc} \tag{13}$$

where e = electronic charge, m = electron mass, h = Planck's constant, c = speed of light.

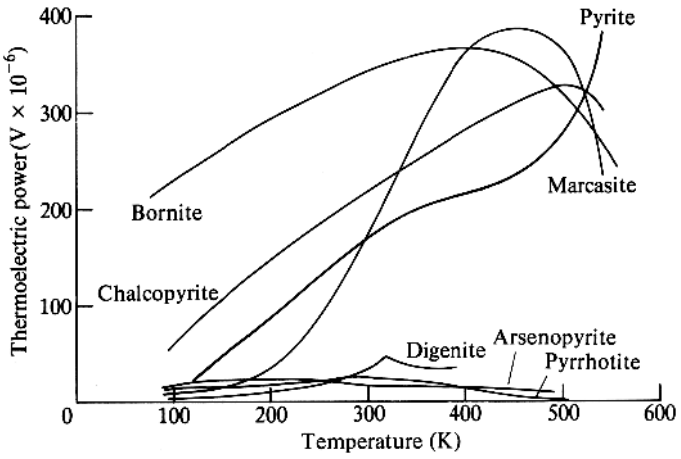

Figure 5. Thermoelectric power versus temperature for several sulfides. Modified after Baleshta and Dibbs (1969).

Table 2. Electrical and Magnetic properties of pyrite-type sulfides.

Compound	Electrical Properties[a]			Magnetic Properties[b]		
	Resistivity at 25 °C (ohm cm)	**E_a (eV)**	**Seeback Coefficient (μ V deg^{-1})**	**Susceptibility at 25 °C (× 10^6 c.g.s. units mole^{-1})**	**Magnetic Moment (μ_{eff}) (μ_B)**	**T_N, T_c or θ**
MnS_2 (hauerite)	—	Semiconducting (1)	—	Paramagnetic/ antiferro-magnetic (1)	~6.3 (3)	T_N = 48.2 K (4)
FeS_2 (pyrite)	1.74 (2)	Semiconducting 0.20 (298 K) (2) 0.46 (500 K)	−500 (2)	Diamagnetic ~ 10 (9)	0 (2)	—
CoS_2 (cattierite)	2×10^{-4} (2) (for $CoS_{1.99}$) 7.6×10^{-6} at 4.2 K (8)	Metallic (2)	−28 (2)	Paramagnetic/ ferromagnetic 4000 (9)	~1.84 (2)	T_c = 110 K (2) θ = 193 K
NiS_2 (vaesite)	6×10^{-1} (2) (for $NiS_{1.99}$)	Semiconducting 0.25 (500 K) (5) 0.12 (298 K) (2) 0.32 (500 K)	+311 (2)	Paramagnetic 700 (9)	~3.2 (6) ~2.48 (9)	θ = −1500 K (6) −740 K (9)
CuS_2	1.5×10^{-4} (2)	Metallic (2) Superconducting <1.56 K (7)	+3 (2)	0.29 (2) Pauli paramagnetic ~40 (9)	—	—
ZnS_2	1.0×10^6 (2)	Semiconducting (2) ~2.5		Diamagnetic -0.36 emu g^{-1} (2)	—	—

References: (1) Hulliger (1968); (2) Bither et al. (1968); (3) Hastings et al. (1959); (4) Lin and Hacker (1968); (5) Hulliger (1959); (6) Benoit (1955); (7) Bither et al. (1966); (8) Butler and Bouchard (1971); (9) Adachi et al (Adachi et al. 1969).

Notes: [a] E_a, activation energy (eV).

[b] μ_{eff}, magnetic moment (in Bohr magnetons; μ_B); T_N Néel temperature; T_C, Curie temperature; θ, Weiss constant

However, this is not the magnetic moment of a single electron, since the complete quantum mechanical treatment is more complex. In fact, the magnetic moment μ_s of a single electron is given from wave mechanics as:

$$\mu_s \text{ (in } \mu_B) = g\sqrt{s(s+1)} \tag{14}$$

where s is the spin quantum number and g is the gyromagnetic ratio which relates the angular momentum of the electron, $[s(s+1)]^{½}$, to the magnetic moment ($g = 2$ for a spin only moment). From Equation (14), the spin magnetic moment of one electron is calculated to be $1.73\mu_B$ from the electron spin alone. This may be reduced or augmented by an orbital contribution. What is significant to this discussion is that knowledge of the magnetic moment (μ_{eff}) of a paramagnetic ion or atom in a compound provides information on the number of unpaired electrons on that atom or ion. Magnetic moments cannot be directly measured; the material property normally measured is the magnetic susceptibility χ where:

$$M = \chi H \tag{15}$$

in which M is the intensity of magnetization and H is the applied field intensity. In the simplest case, the magnetic moment is related to the susceptibility:

$$\mu_{eff} = \left(\frac{3k}{N_A \mu_B{}^2}\right)^{½} (\chi_A T)^{½} = 2.828(\chi_A T)^{½} \tag{16}$$

where K = Boltzmann's constant; N_A = Avogadro's number; μ_B = Bohr magneton; χ_A = magnetic susceptibility per gram atom; T = temperature (K). The measurement of magnetic susceptibility will be further discussed below.

An important aspect of the study of magnetic properties is their variation as a function of temperature. Diamagnetism (for which χ is negative) does not vary in magnitude with temperature, whereas the qualitative temperature dependence of magnetic susceptibility for a simple paramagnetic is shown in Figure 6(a). Curie demonstrated that paramagnetic susceptibilities depend inversely on temperature and may follow the simple law:

$$\chi_m{}^{corr} = \frac{C}{T} \tag{17}$$

where $\chi_m{}^{corr}$ is paramagnetic susceptibility per mole corrected for the diamagnetism due to closed shells; T is the absolute temperature; and C is a characteristic constant for the substance (Curie constant). If T is plotted against $1/\chi_m{}^{corr}$ for a paramagnet which obeys this Curie law

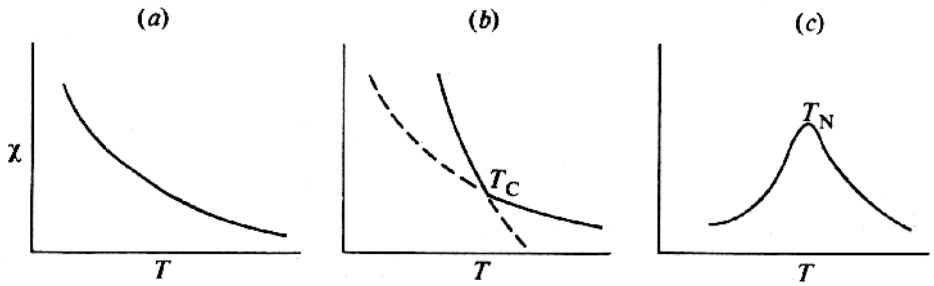

Figure 6. The qualitative temperature (T) dependence of magnetic susceptibility (χ) in (a) a simple paramagnet, (b) a ferromagnet and (c) an antiferromagnet. T_c, Curie temperature. T_N, Néel temperature. Modified after Cotton and Wilkinson (1972).

(Eqn. 17), a straight line of slope C should be obtained which intersects the origin. Although many paramagnetic substances do show this behavior, there are many others for which this line does not go through the origin but cuts the temperature axis above or below 0 K. Such behavior can be represented by a modification of Equation (17):

$$\chi_m^{corr} = \frac{C}{T - \theta} \tag{18}$$

in which θ is the temperature at which the line cuts the T axis. This equation expresses the Curie-Weiss law and θ is the Weiss constant. This complication arises because the magnetic dipoles of individual atoms or ions are not independent of each other. It also results in a more complex relationship between susceptibility and magnetic moment than shown in Equation (16).

In addition to simple paramagnetism, there are four other forms of paramagnetism, several of which are particularly important in the metal sulfides. These are ferromagnetism, antiferromagnetism, ferrimagnetism, and Pauli paramagnetism, all of which arise through the interaction of unpaired electrons on neighboring "paramagnetic" ions. A spontaneous alignment of magnetic moments in the same direction occurs in ferromagnetic materials and is retained even after the external magnetic field has been removed. The resulting permanent magnetization (as in metallic iron) is attributed to a quantum mechanical exchange interaction between the electrons and adjacent atoms. The efficiency of this interaction (and therefore the value of the susceptibility) decreases with increasing temperature, breaking down at the Curie temperature (T_c) above which such materials exhibit simple paramagnetic behavior (Fig. 6b).

In antiferromagnets, the moments spontaneously align themselves but are antiparallel on adjacent atoms, so that they cancel and result in no net moment. Such antiferromagnetic coupling frequently takes place between two paramagnetic metal cations via an anion intermediary. A number of mechanisms have been proposed (see Fig. 7) to account for antiferromagnetism and ferromagnetism in ionic solids such as metal sulfides:

(1) *Superexchange*. For example, one of the two 3*p* valence electrons of S^{2-} could be transferred to the half-filled shell of a transition metal ion (*M*, e.g., Mn^{2+} with five *d* electrons) and according Hund's rule its spin would be antiparallel to the spins of the five *d* electrons. The second sulfur *p* electron would have its spin antiparallel to the first (because of the Pauli exclusion principle) and would remain localized on the sulfur ion. Such a configuration can also be formed with the opposite metal ion, antiparallel alignment of unpaired electrons on the two metal ions shown in Figure 7 results. The same mechanism predicts ferromagnetic coupling for cations with less than half-filled shells. The superexchange interaction clearly depends on orbital overlap and is strongest for a linear *M*-S-*M* arrangement and weakest when the *M*-S bonds are at right-angles.

(2) *Indirect exchange* is similar to superexchange but transfer (or "promotion") of a sulfur *p* electron to the *d* shell of the overlapping cation is not involved. Here the two 3*p* electrons of the sulfur atom simultaneously participate in antiferromagnetic coupling by remaining in their orbits but occupying areas near the metal ions to which they are coupled in antiparallel alignment. The coupling is always antiferromagnetic.

(3) *Double exchange* is suggested for systems containing mixed valence states and involves a simultaneous transfer of electrons from cation to sulfur and sulfur to cation. Ferromagnetism always results.

(4) *Semi-covalent exchange* is a modification of superexchange which assumes appreciable covalent character in the metal-anion bond; distribution of electrons amongst hybridized orbitals leads to formation of electron pair bonds between the central anion and adjacent cations which are thus antiferromagnetically coupled.

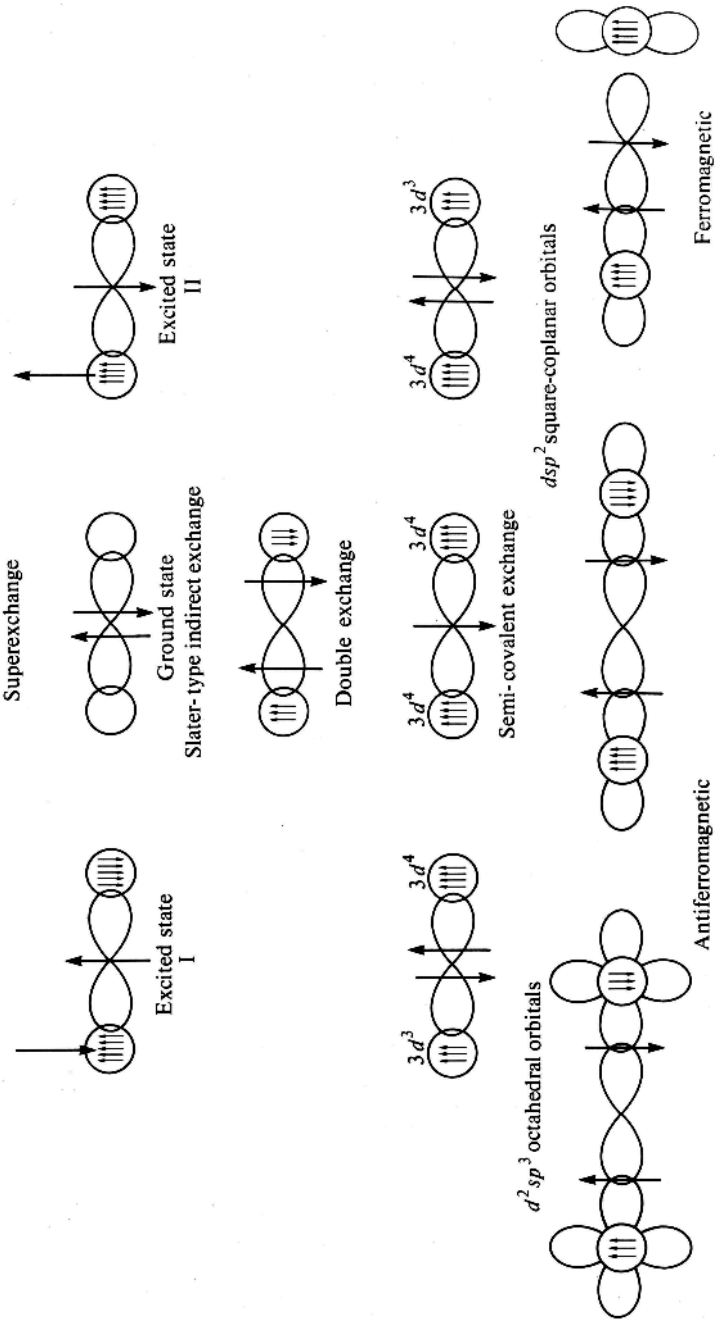

Figure 7. Schematic representation of different types of exchange mechanisms. After Schull and Wollan (1956).

Examples of exchange interaction in a sulfide system are afforded by the magnetic structures of the three polymorphs of MnS—the NaCl structure-type (alabandite) and the sphalerite and wurtzite analogs. In each case, the Mn^{2+} cation has 12 nearest Mn^{2+} neighbors but different numbers of S^{2-} anion neighbors. In alabandite, Mn^{2+} is bonded to next-nearest-neighbor Mn^{2+} ions via 180° sulfur *p* orbitals, whereas in the other polymorphs the linkage is tetrahedral. The magnetic structures determined by neutron diffraction, after Corliss et al. (1956) are shown in Figure 8. In the alabandite structure, the nearest Mn^{2+} neighbors are antiferromagnetically coupled by superexchange via the sulfur intermediaries, whereas in the sphalerite and wurtzite structure-types, next-nearest-neighbors are coupled. The magnetic structure of chalcopyrite ($CuFeS_2$) is closely related to sphalerite-type MnS.

It is characteristic of antiferromagnetic materials that their magnetic susceptibility increases with temperature over the range of antiferromagnetic behavior up to the Néel temperature (T_N), above which normal paramagnetic behavior is exhibited with decreasing susceptibility as temperature increases (see Fig. 6c).

From the discussion of exchange mechanisms giving rise to ferromagnetism and antiferromagnetism, it can be seen that the possibility exists of materials in which both types of interaction occur simultaneously. Such materials do occur and are known as ferrimagnets. The best known material exhibiting this phenomenon is magnetite (Fe_3O_4). Greigite (Fe_3S_4), the sulfur analogue of magnetite, is also ferrimagnetic. Another important example is provided by monoclinic pyrrhotite (Fe_7S_8), in which metal atom vacancies on one of the magnetic sublattices result in imbalance and consequent ferrimagnetism.

The last type of paramagnetism, Pauli paramagnetism, is found only in metallic materials in which the outermost electrons are extensively delocalized. Here, in a partly filled band, application of an external field causes imbalance between spin-up and spin-down electrons and hence a net magnetic moment. Such susceptibility values are very small and are independent of temperature.

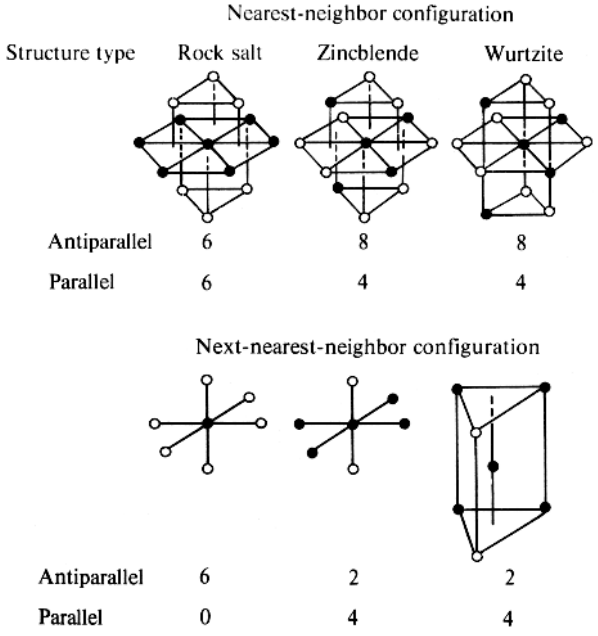

Figure 8. Magnetic structures of the three polymorphic forms of MnS showing nearest- and next-nearest-neighbor spin configurations. Only metal atoms are shown, and open and closed circles represent up and down spins respectively. [Used with permission of APS from Corliss et al. (1956), *Physical Review*, Vol. 104, Fig. 2, p. 925.]

Measurement of magnetic properties

The measurement of magnetic susceptibility is the most important technique in characterizing a substance magnetically. Conventional methods depend on measuring the force exerted on the sample when it is placed in an inhomogeneous magnetic field. For example, in the Guoy balance, a cylindrical sample is suspended between the pole pieces of an electromagnet and the weights of the sample in zero field and in a known magnetic field are recorded. A paramagnetic sample will be attracted by the field (or diamagnetic sample repelled) resulting in an apparent change in the mass of the sample (Δm) then:

$$\Delta m = \tfrac{1}{2}\, \kappa\, H^2 A \tag{19}$$

where H is the field strength at the center (in Oesteds); A is the cross-sectional area of the sample and κ is its volume susceptibility. κ is converted to the susceptibility per gram by dividing by the sample density, and then to the susceptibility per mole by multiplying by the molecular weight. Other magnetic balances apply similar principles and by the addition of Dewar and heating coil systems, susceptibility can be studied as a function of temperature and Curie and Néel points can be determined.

In the case of ferri- or ferromagnetic materials, the intensity of magnetization (I) increases markedly with increase of the applied field up to a certain value at which saturation magnetization is reached. Determination of the saturating field and the study of magnetization as a function of applied field is another important application of the magnetic balance, particularly in relation to paleomagnetic work (McElhinny 1973).

A very sensitive commercially available laboratory instrument for measuring anisotropy of magnetic susceptibility and bulk magnetic susceptibility, at high and low temperatures and in weak variable magnetic fields (field range from 2 A/m to 700 A/m, peak values), particularly in the area of rock magnetism, is the Kappa Bridge. This system works by measuring the change in the induction properties of a bridge circuit with and without the sample (the sample is automatically lifted in and out of the sensor unit).

SQUID magnetometry. Currently the SQUID (Superconducting QUantum Interference Device) magnetometer is the most sensitve magnetic sensor available to study the magnetic properties of solids. The sensitivity of the SQUID magnetic sensor makes it possible to measure the magnetic response of a material (in the 10^{-15} tesla range) in its proper field without significant disturbance of the magnetic moments by external magnetic fields. The SQUID magnetometer measures magnetic field variations using a thin electrically resistive junction (the Josephson junction) between two superconducting electromagnets (Fig. 9) (O'Connor 1982). The SQUID sensing coil surrounding the sample is cooled using liquid helium down to its superconducting temperature and a current is passed through while the voltage across the junction is monitored. The magnetization of the sample changes the magnetic flux through the sensing coil which acts as an amplifier and is recorded as a variation in the output signal. The high sensitivity, fast response time and high field of the superconducting magnets, along with the ability to examine samples over a temperature range, mean it is an excellent tool for examining mineral samples with small magnetic moments as they pass through various structural transformations, or with variations in composition. In dilute magnetic semiconductors (such as transition metal doped ZnS) where small amounts of paramagnetic species are present, this sensitivity is particularly important. Drawbacks include sensitivity to outside noise and vibrations, expense, and the fact the SQUID measures variations in field so that samples need to move in and out of the coils to establish a baseline. To date, SQUID investigations of sulfides have been relatively few, but see Brun del Re et al. (1992) and Di Benedetto et al. (2002).

Electron paramagnetic resonance (EPR) can be employed with a SQUID detection system to quantitatively measure the change in magnetic moment of a specimen at different values of

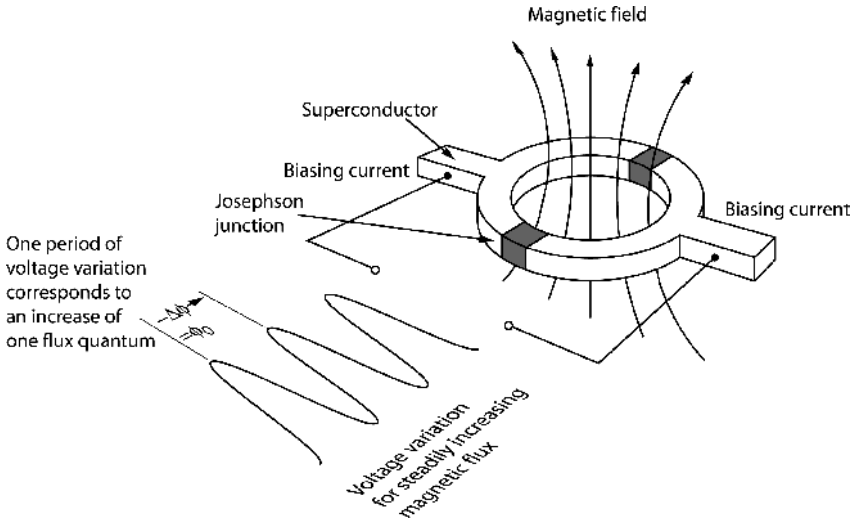

Figure 9. Diagrammatic representation of a SQUID magnetometer showing a superconducting loop interrupted by Josephson junctions. After Nave (2000).

applied magnetic field. EPR measurements of metal sulfides are briefly discussed elsewhere in this volume (Wincott and Vaughan 2006, this volume).

***X-ray magnetic circular dichroism* (*XMCD*).** XMCD is a recently developed analytical technique that utilizes the differences in X-ray photoabsorption that occurs near X-ray absorption edges when circularly polarized light is incident on a magnetized sample, and either the alignment of the light helicity or the magnetization direction is reversed (Thole et al. 1985; van der Laan et al. 1986; Schutz et al. 1997). It can be used to provide information about the electronic and magnetic structure of ferromagnetic and ferrimagnetic solids by tuning the X-ray energy through the absorption edges that excite electrons to the valence band responsible for magnetism. Although it has largely been employed in the study of magnetic thin films and multilayers, it can just as easily be used on mineral powders, slices or orientated samples. In particular, it has been used extensively on magnetic oxides (such as the ferrite spinels and garnets), dilute magnetic semiconductors and magnetic nanostructures (van der Laan et al. 1986; van der Laan and Thole 1991; Chen et al. 1995; Stöhr 1995; Schutz et al. 1997). Even though little used on sulfides so far, the search for new magnetic materials, including nanomaterials and thin film multilayers containing chalcogenides, means it is becoming an increasing important technique for the mineral physicist (Pearce et al. 2006b).

XMCD utilizes the tunability of synchrotron sources and the element specific property of X-ray absorption spectroscopy (XAS) that allows the investigator to focus on the contribution of specific elements in chemically complex materials. It can potentially provide information about the oxidation state (including mixed states), site symmetry, spin state and crystal-field splitting of the absorbing 3*d* transition metal ions. XMCD is also sensitive to the direction and size of the local magnetic moments. In the 3*d* transition metals the magnetic moments (spin and orbital) are almost entirely derived from the 3*d* electrons and, therefore, the most effective way to examine magnetic materials using XAS is by observing the excitation of 2*p* core electrons to unfilled 3*d* states by analysis of the $L_{2,3}$ edge absorption.

In samples subjected to circularly polarized light, the polarized photons transfer angular momentum to the excited electron and, because of the usually large spin-orbit coupling, this is

transferred to both the spin and orbital components of the electron. At the L_3 absorption edge ($2p_{3/2}$) light polarized in one direction will preferentially excite electrons parallel (arbitrarily "spin up") to the polarized photons compared to those antiparallel ("spin down"), whereas at the L_2 absorption edge ($2p_{1/2}$) in the initial state, spin down electrons will be preferentially excited (Fig. 10). If either the light polarization or the magnetic field is reversed, it has the opposite effect on the $2p_{3/2}$ and $2p_{1/2}$ electrons; the difference between the two spectra is determined by the empty states available in the valence band and can be related to the spin and orbital components of the magnetism (see Thole and van der Laan 1988 and van der Laan and Thole 1988 for details).

The sum rule, developed by Thole et al. (1992), states that the XMCD signal integrated over the 2*p* absorption edge is proportional to the orbital part of the 3*d* magnetic moment per hole. The weighted difference of the integrated XMCD signals of the L_3 and L_2 edge provides the spin moment per hole. Therefore, if the number of holes in the electronic state is known, or can be estimated, the absolute magnetic moments for individual atoms can be derived (van der Laan and Thole 1991).

Since the cross-section for soft X-ray absorption is very high, samples in the form of very thin films would be required for transmission measurement. Instead, measuring the photoabsorption in the soft X-ray regime is better done by recording the total electron yield (TEY) as the photon energy is scanned across the absorption edge (Fig. 11a,b). However this method is inherently surface sensitive due to the limited escape depth of the electrons

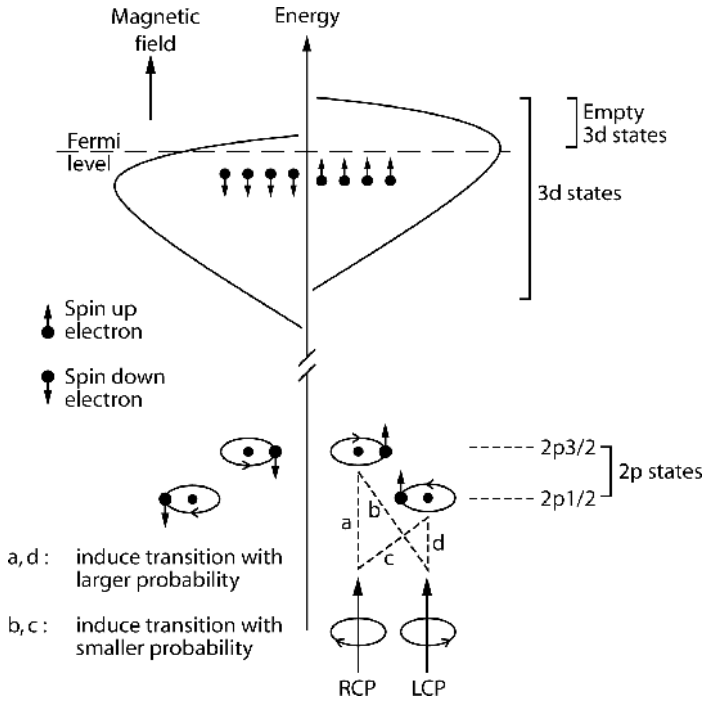

Figure 10. Diagrammatic representation of the XMCD effect. The arbitrarily assigned 'spin up' and 'spin down' electrons in a mineral containing unpaired electrons are not equal and if the applied magnetic field or light helicity are in the 'up' direction there is a high probability that the 'up spin' electrons will be excited from 2*p* to 3*d*. If the orbital motion of the 2*p* electrons in the same sense as circular motion of light the transition is larger and the L_3 peak is enhanced; change the magnetization direction or the polarization of the light, and the effect is reversed. [Reproduced with kind permission of Ian Kirkman.]

(typically ~20-50 Å for the energy region of the transition metal L-edges). It is, therefore, vital that surface oxidation/contamination is avoided in order for meaningful results to be obtained. Also the measurement will give the absorption spectrum averaged over all contributions within the sampling depth, and even a small surface oxidation will contribute to the total spectrum. The fluorescence yield (FY) signal can also be used to measure the XAS and can be collected simultaneously. This signal is less surface sensitive; however, the fluorescence rate in the soft X-ray region is rather low and FY shows a lower signal to noise ratio than TEY. Magnetic reversal is achieved by "flipping" the magnetization of the sample using an electromagnet (Pattrick et al. 2002) and computer controlled action is undertaken for every energy step across the absorption edge. The two resulting spectra are normalized and then the difference spectrum produces the XMCD spectrum. Spectra can also be derived scanning firstly with one magnetization direction and then in the reverse direction, but variations in beam characteristics can lead to loss of fine structure and normalization problems.

The effectiveness of XMCD for sulfide minerals is well demonstrated by greigite (Fe_3S_4). Figure 12 (Letard et al. 2005) shows the isotropic Fe $L_{2,3}$ absorption spectra of natural greigite collected by reversing the applied 2 Tesla magnetic field. The sample need not be aligned along any specific direction and, although the strength of the applied field changes the shape of the spectra measured with positive and negative magnetization, it does not change the shape of the XMCD, only its magnitude. In the case of greigite, the three peaks relate to the contributions from Fe in the tetrahedral lattice site and Fe in two oxidation states in the octahedral lattice site. To separate the contributions of Fe^{2+} and Fe^{3+} in the octahedral and tetrahedral sites an approach similar to that employed for the oxide, magnetite, is used (van der Laan and Kirkman 1992; Pattrick et al. 2002). However, in iron sulfides the covalence of the bonds is stronger than in oxides, implying that the multiplet structure will be less visible and the selectivity of site and oxidation state will be less precise (Letard et al. 2005).

Neutron diffraction. As neutrons interact more strongly with atomic nuclei than X-rays, they are better than either diffracted X-rays or electrons in determining atomic positions. They also interact less with solid materials and, as a result, cause much less damage than X-rays. In magnetic studies, neutron diffraction is particularly valuable because the neutrons have a small magnetic moment and, therefore, interact with the spin and orbital magnetic moments of unpaired electrons in solid phases, and they are sensitive to magnetic ordering. Neutrons are being increasingly used by mineralogists, although the requirement for relatively large sample sizes (a few grams) and for sample homogeneity have meant using synthetic phases. Excellent reviews can be found in Harrison (2006) and Dove (2002). New generations of neutron instruments (e.g., GEM at ISIS, UK) and neutron sources e.g., Spallation Neutron Source (SNS) at Oakridge, Tennessee <*http://www.sns.gov/*> will mean that smaller samples can be used, with powder diffraction performed on samples of the order 10-100 mg.

A beam of neutrons can be diffracted by interaction with crystalline materials. Neutrons are either produced continuously by nuclear reactors or by both continuous and pulsed spallation sources. The world's most powerful neutron source is the SNS, where negatively charged hydrogen ions comprising a proton and two electrons are injected into a linear accelerator and accelerated up to energies of 1 G eV. The ions are stripped off the electrons as they pass through a foil and the resulting protons enter a ring where they form bunches. These proton bunches are ejected from the ring as a pulse to strike a liquid mercury target, producing neutron pulses by the resulting spallation. The neutron pulses are slowed by a "moderator" and guided into beamlines where neutrons of specific energies can be selected for a range of experiments. Water moderators are used to produce room temperature neutrons and liquid nitrogen to produce cold (20 K) neutrons.

The neutrons hitting a sample have a range of energies and wavelengths and neutrons are diffracted when atomic distances and wavelengths match. Magnetic neutron diffraction occurs

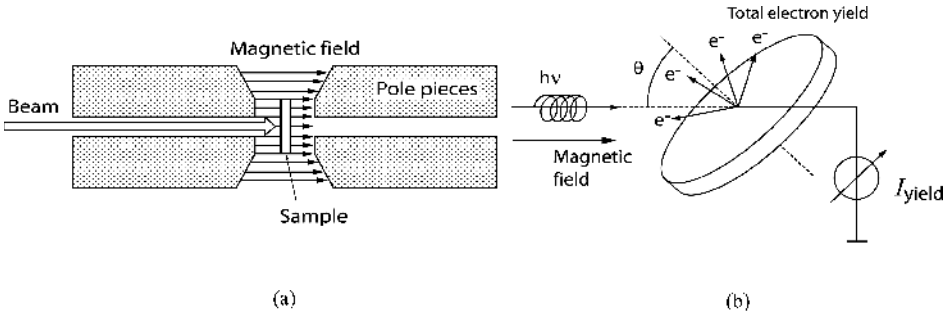

Figure 11. Diagrams showing (a) XMCD sample set up and (*b*) measurement of total electron yield.

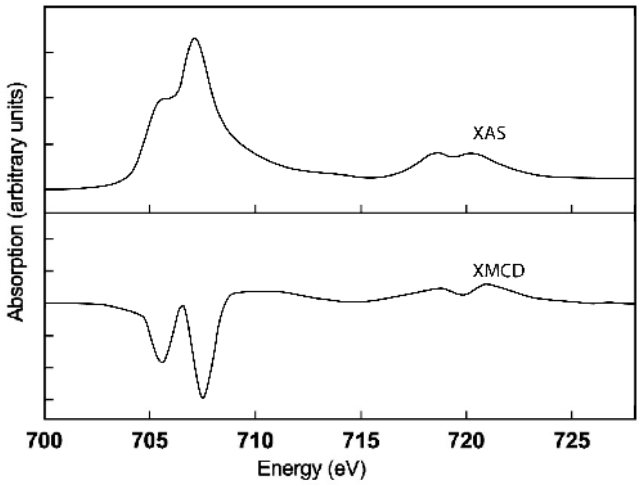

Figure 12. Fe $L_{3,2}$ absorption and XMCD spectra of natural greigite. The spectra were collected in a reversible 0.6 Tesla magnetic field, and the resulting XMCD difference spectrum is shown below (intensity scale enhanced by a factor of three). (Letard et al. 2005).

as a result of the interaction between the magnetic moment of the neutron and the magnetic moment of the target atom (μ). The magnetic moment of the atom is derived from the unpaired electron "cloud" and interferences from contributions from different parts of the cloud mean that magnetic diffraction reduces with an increasing angle to the scattering vector (Q). Thus, magnetic contributions are seen in diffraction spectra at low values of 2θ. Neutron diffraction is only sensitive to $\mu_\perp$ which is the component of the atomic magnetic moment perpendicular to the scattering vector (Q). Unlike the nuclear (crystal) structure contribution, which remains constant as a function of Q, the magnetic contribution to a neutron diffraction pattern is restricted to small Q. Hence, the magnetic contribution to a Bragg diffraction peak will be exactly zero if the moments are normal to the diffracting planes (Fig. 13).

Multi-collectors are used to detect the intensity of the diffracted neutrons as a function of angle for fixed wavelength experiments, or intensity as a function of time-of-flight for spallation source experiments (time of flight is related to the velocity, which is related to the energy), thus generating a diffraction pattern of peaks and intensities (Rodríguez-Carvajal 1993). The "magnetic" atoms in the (mineral) phase form a magnetic lattice that contributes

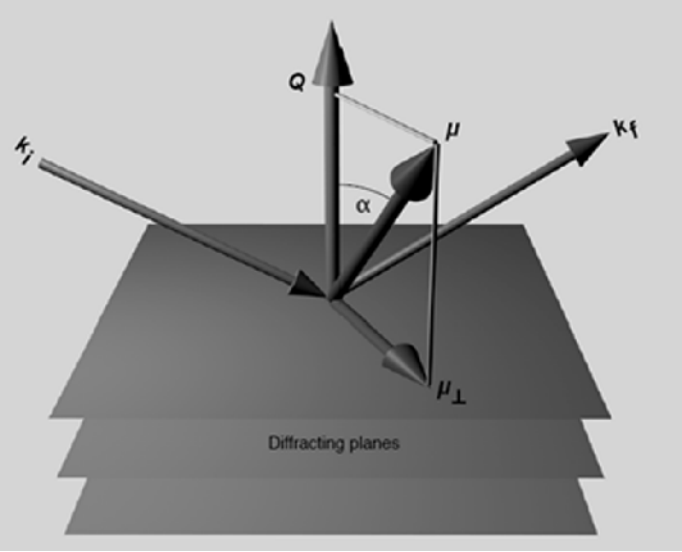

Figure 13. Diagrammatic representation of the angular relationship between scattering vector and magnetic interaction vector for magnetic neutron scattering. The incident and scattered neutron beams are described by the wave vectors k_i and k_f. The scattering vector, Q, is defined as $Q = k_f - k_i$. For Bragg diffraction, Q points normal to the set of diffracting planes. The magnetic moment of the atom is defined by the vector μ. The scattering amplitude is determined by the component of μ perpendicular to Q ($\mu_\perp$). (Harrison 2006).

to the diffraction pattern. In general, the periodicity of the magnetic structure will be different from the nuclear structure, leading to the presence of magnetic superlattice peaks. The magnetic and nuclear reflections coincide, however, when the nuclear and magnetic unit cells are equal. Figure 14 shows the neutron diffraction pattern of α-MnS taken at 4.2 K and a wavelength of 1.064 Å. The diffraction peaks labeled "nuclear" are the fundamental peaks and persist unchanged above the Neél temperature. The superstructure peaks are entirely magnetic in origin and disappear when the Neél temperature is exceeded (Corliss et al. 1956). These magnetic superstructure peaks are evident in the neutron diffraction patterns for all three polymorphs of MnS, indicating three distinct antiferromagnetic structures. The nearest and next-nearest neighbor configurations for the three forms of MnS are shown in Figure 8. The magnetic diffraction by the individual atoms is sensitive to the relative orientation of the neutron magnetic moment, the atomic magnetic moment, and the scattering vector (Harrison 2006). The diffraction trace will, thus, comprise both nuclear structure and magnetic structure components and, for unpolarized neutrons, it is the sum of the nuclear and magnetic contributions. By using polarized neutrons, the magnetic component can be separated from the nuclear component. When the polarization direction is set parallel to the scattering vector, magnetic diffraction will always flip the polarization of the incident beam whereas nuclear diffraction preserves the polarization of the beam. By analyzing the spin-flip versus non-spin-flip intensities, the two signals can be separated.

Elastic scattering arises from the static component of a crystal structure and therefore has zero angular frequency but is not identical to the scattering function. The main information obtained from elastic studies is the magnetic structure including the direction and the magnitude of the magnetic moments for each magnetic atom. The vibration of atoms about their mean positions, as in a crystalline solid, results in inelastic scattering. Inelastic neutron

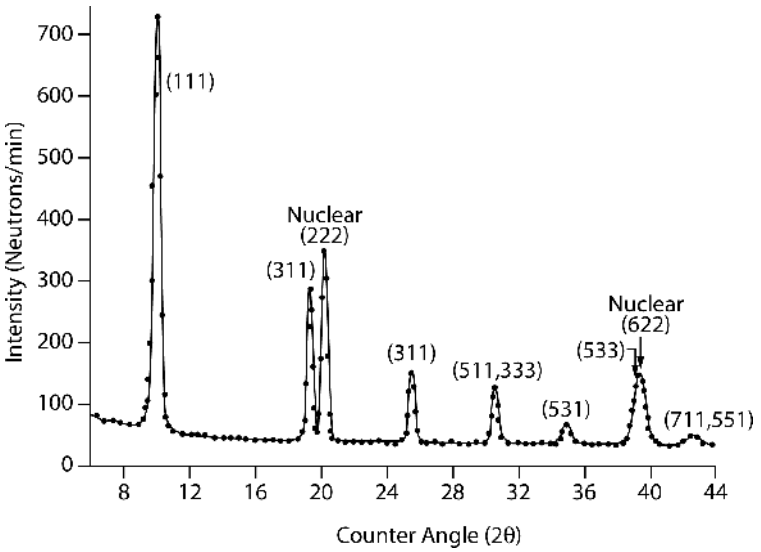

Figure 14. Neutron diffraction pattern of MnS - rock salt structure (Temperature = 4.2 K, wavelength = 10.423 Å) (Corliss et al. 1956).

scattering can be used to study magnetic dynamics or spin waves, which give an indication of the strength and nature of the exchange forces between neighboring spins (Dove 2002).

ELECTRICAL AND MAGNETIC PROPERTIES OF METAL SULFIDES

All sulfides of main group (i.e., non-transition) elements (including Zn, Cd, Hg) are diamagnetic insulators or semiconductors. This is because, in terms of a simple band structure model, the valence and conduction bands are, respectively, filled and empty and do not overlap. Such situations are shown in Figure 1a,b. Generally, the valence band in such compounds should be largely made up of S 3*p* and 3*s* type orbitals and the conduction band of metal *s* and *p* orbitals. Galena (PbS) and sphalerite (ZnS) are the two most important examples of this group of sulfides.

The sulfides of the transition metals can be considered as intermediate between the transition metal oxides, whose properties are determined by strong electronic correlation effects, and the transition metal selenides, showing a variety of electronically induced structural phase transitions. Transition metal sulfides have many technological applications, ranging from lubricants to catalysts, motivating the need to develop an understanding of their properties at an atomistic level (Hobbs and Hafner 1999). In the transition metal sulfides, the electronic structures, and hence electrical and magnetic properties, are complicated by the presence of the *d* electrons (Jellinek 1972). The implications are best examined by simple molecular orbital/band model approach including the *d* electrons (for further discussion, see Vaughan and Rosso 2006). In Figure 1c-h, valence and conduction band energy levels comprised of metal and sulfur *s* and *p* orbitals are shown with *d* orbital energy levels added. Separations in the range of one to several electron volts are expected between *s*-*p* valence and conduction bands, but the relative energy of the *d* orbital levels may vary widely as shown in the figure. Also, most importantly, the *d* orbitals may overlap with sulfur orbitals or even with the *d* orbitals of adjacent metals to form a band (or bands), or may not overlap at all; i.e., remain localized. When overlap produces delocalization of the *d* electrons, the resulting bands are usually narrow. In Figure 1c, localized

d electrons occur between the *s-p* valence and conduction bands in energy, so the material is a semiconductor. If the *d* electrons are completely paired, the material will be diamagnetic (e.g., pyrite, FeS_2); if not, then it will exhibit temperature-dependent paramagnetism (e.g., hauerite, MnS_2) and may be magnetically ordered over a certain temperature range. The *d* levels in Figure 1d,e are also localized but below the top of the valence band in energy. If Figure 1d applies, the material will again exhibit semiconduction and diamagnetism or paramagnetism. However, if the energy of the *d* orbitals of the same cation (T^{M+}) but in a different oxidation state ($T^{(M-1)+}$) also fall below the top of the valence band, as in Figure 1e, then the cation will be reduced by the removal of an electron from the valence band. The holes created in the valence band permit *p*-type metallic conduction. Thus, the material will be metallic but exhibit paramagnetism. Similar properties may be shown by a sulfide of the type illustrated in Figure 1f where the localized *d* levels overlap the empty conduction band. When an electric field is applied, transfer of electrons to the conduction band occurs, producing *n*-type metallic conductivity (CoS_2, cattierite, exhibits behavior akin to this). Finally, in the sulfides illustrated in Figure 1g,h, the *d* levels are delocalized to form a narrow band near the top of the *s-p* valence band or in the band gap. If such a narrow band is partly filled, the sulfide will exhibit metallic conductivity and Pauli paramagnetism or diamagnetism (Co_3S_4, linnaeite, and a number of metal-rich sulfides exhibit such behavior).

The above discussion offers a simple model to explain the diversity of sulfide magnetic and electrical properties. However, it should be noted that in this discussion the *d* electrons have been regarded as degenerate (equal in energy). Of course, in all sulfides the degeneracy of the *d* orbitals is partly removed by the ligand field of the surrounding sulfur atoms (Vaughan and Rosso 2006, this volume). This leads to further complexities; e.g., the t_{2g} levels of an octahedrally coordinated transition metal ion may remain localized and the e_g levels overlap to form a narrow band. Such situations will be discussed in following sections, but they do not invalidate the broad categories outline above, which were originally organized into four classes of transition metal sulfide by Jellinek (1972):

(A) Semiconductors with paramagnetism or diamagnetism i.e., localized *d* electrons, see Figure 1c,d.

(B) Metallic conductors of *p*-type with paramagnetism i.e., localized *d* electrons, see Figure 1e.

(C) Metallic conductors of *n*-type with paramagnetism i.e., localized *d* electrons, see Figure 1f.

(D) Metallic conductors with Pauli paramagnetism i.e., delocalized *d* electrons, see Figure 1g,h.

The magnetic and electrical data available for several major sulfides and groups of sulfides will now be considered, beginning with the sphalerite- and wurtzite-type metal sulfides, including ZnS. The effect of adding a transition metal to such a material will then be considered using data on (Zn,Fe)S, and other sulfides of this structure type will also be discussed. The series of pyrite-type sulfides provides a good example of an isostructural series involving successive addition of electrons and the NiAs-type sulfides an opportunity to consider a group of materials with complex magnetic ordering behavior. Also discussed are galena (PbS) and alabandite (α-MnS) with their simple halite-type structures, and a number of other phases (makinawite, smythite and greigite) of interest because of their geochemical or rock magnetic importance. A summary of the magnetic and electrical properties of these important sulfides is provided in Table 3. Shuey (1975) has also reviewed the electrical properties of many mineral sulfides and discussed their interpretation in detail. This includes sulfides with a range of different properties from sphalerite (ZnS), which is a notoriously poor electrical conductor with a wide band gap (~3.5 eV); to covellite (CuS), which has very high

Table 3. Electrical and magnetic characteristics of some common sulfides. After Corry (2005) and Vaughan and Craig (1978).

Mineral	Formula	Structure	Resistivity (ohm m)	T_C (or T_N where shown) in °C	Magnetic Property; Magnetic susceptibility in $k \times 10^{-6}$cgs
Acanthite	Ag_2S	Ortho.	semiconductor *n*-type; 1.5×10^{-3} to 1.5	179	diamagnetic; $K = -30$
Alabandite	MnS	Cubic	semiconductor	T_N −121	antiferromagnetic; $K = 5{,}600$
Arsenopyrite	FeAsS	Ortho.	semiconductor mixed type; 10^{-5} to 20	<500; (Trans. to Hex at 103)	diamagnetic or paramagnetic; $K = 240$
Bismuthinite	Bi_2S_3	Ortho.	semiconductor *n*-type; 3 to 5.7×10^{4}	50	diamagnetic; $K = -123$
Bornite	Cu_5FeS_4	Ortho.	semiconductor *p*-type; 10^{-5} to 1.6 large decrease at $T \sim 228$	<228; T_N −265	paramagnetic; anitferromagentic (1) below −197
Chalcocite	Cu_2S	Mono.	semiconductor *p*-type; 10^{-4} to 2.3×10^{3}	103 to 130; (Trans. to Hex. at 103)	diamagnetic
Chalcopyrite	$CuFeS_2$	Tetrag.	semiconductor *n*-type ; 10^{-5} to 150; large decrease at $T \sim 330$°C	<550; T_N 277	antiferromagnetic; k~32
Cinnabar	HgS	Hex.	semiconductor; 10^{9} to 10^{11}	<344	diamagnetic; $K = -55$
Covellite	CuS	Hex.	*p*-type metal; 10^{-7} to 10^{-3}	<500	diamagnetic; $K = -2$
Enargite	Cu_3AsS_4	Ortho.	semiconductor *p*-type; 2×10^{-4} to 0.9	<383	diamagnetic
Galena	PbS	Cubic	semiconductor mixed type; 6.8×10^{-6} to 17.5 (z mean 2×10^{-3})	1127	diamagnetic; $K = -3$ to +84
Greigite	Fe_3S_4	Cubic	metal?		ferrimagnetic
Mackinawite	$Fe_{1+x}S$	Tetrag.	metal		pauli paramagnetic
Marcasite	FeS_2	Ortho.	semiconductor *p*-type; 10^{-3} to 10^{4}. large decrease at T~200°C.	<520	diamagnetic $k \sim 18{,}720$
Metacinnabar	HgS	Cubic	semiconductor; 10^{-6} to 10^{-2}		diamagnetic; $K = -55$
Molybdenite	MoS_2	Hex.	semiconductor mixed type; 10^{-3}6	<1675	diamagnetic; $K = -63$ to −77
Pentlandite	$(Fe,Ni)_9S_8$		metal		Pauli paramagnetic
Pyrrhotite	Fe_7S_8	Mono.	*p*-type metal; 10^{-6} to 10^{-1}	315	ferrimagnetic; ($k = 10^{2}$ to 5×10^{5} mean 1.25×10^{5})
Pyrrhotite	$Fe_{1-x}S$	Hex.	metal	T_N 315	antiferromagnetic
Sphalerite	ZnS	Cubic	semiconductor; 2.7×10^{-3} to 10^{12}	1020	diamagnetic; $K = -25$ to −60
Stibnite	Sb_2S_3	Ortho	semiconductor; 10^{5} to 10^{12}(mean 5×10^{6})	147 to 217	diamagnetic; $K = -86$
Tennantite	$(Cu,Fe,Zn,Ag)_{12}As_4S_{13}$	Cubic	semiconductor; 7×10^{-4} to 0.4		paramagnetic
Tetrahedrite	$(Cu,Fe,Zn,Ag)_{12}Sb_4S_{13}$	Cubic	semiconductor; 0.3 to 3×10^{4}		paramagnetic
Troilite	FeS	Hex.	*p*-type metal; 10^{-6} to 10^{-1}	T_N 315	antiferromagnetic; $K = 5{,}187$
Wurtzite	ZnS	Hex.	semiconductor ; 3.5×10^{2}		diamagnetic; $K = -25$

(1) Collins et al. (1981)

conductivity as a result of the presence of "charge carrier" holes, formed when one electron per three CuS is removed to give electrical neutrality, due to the S-S pairs in the structure that reduce the charge on the sulfur anions (Tossell 1978).

Metal sulfides of sphalerite and wurtzite (ZnS) structure-type

Pure zinc sulfide is a diamagnetic semiconductor, although the band gap is sufficiently large that it is sometimes described as an insulator. The measured specific magnetic susceptibilities of sphalerite and wurtzite are -0.262×10^{-6} and -0.290×10^{-6}emu g^{-1} respectively (Larach and Turkevich 1955), and are in good agreement with the theoretical value calculated from the susceptibilities of the zinc and sulfur ions of -0.30×10^{-6}emu g^{-1} (International Critical Tables 1929). The forbidden energy gap in ZnS has been report between 3.2 and 3.9 eV at 300 K, depending on the method of measurement (Cheroff and Keller 1958; Fok 1963). Pressure reduces the forbidden energy gap of ZnS. Samara and Drickamer (1962) observed that sphalerite undergoes a semiconductor-to-metal transition to become electrically conducting at very high pressures, probably due to a transformation to an NaCl-type structure with large numbers of defects (Rooymans 1963). Substantial discrepancies in the magnitude of the transformation pressure for ZnS reported in the literature occur due to factors such as the different techniques used to identify the transition and the grain size (Jiang et al. 1999). The energy gap is also reduced by cadmium or mercury substitution. The mechanism of intrinsic semiconduction in ZnS may be *p*- or *n*-type, depending on the stoichiometry. Sphalerite and wurtzite are now known not to be true polymorphs; in fact, sphalerite is zinc-deficient and wurtzite sulfur-deficient compared to the stoichiometric compound. Thus *p*-type semiconduction is expected in sphalerite and *n*-type in wurtzite. Studies of the electrical properties of ZnS heated in air and in excess sulfur vapor support these observations (Morehead 1963; Morehead and Fowler 1962).

The presence of transition metal impurities in ZnS has a pronounced effect on the magnetic and electrical properties. Iron (Spokes and Mitchell 1958) and manganese (Brummage et al. 1964) render sphalerite paramagnetic, and paramagnetic copper centers have been observed in ZnS by Holton et al. (1969). Di Benedetto et al. (2002) used electron paramagnetic resonance spectroscopy to study synthetic sphalerite doped with Mn and suggested that two different Mn^{2+} species are present. Brummage et al. (1964) observed that ZnS containing substantial manganese departs from Curie behavior above 77 K. This was attributed to antiferromagnetic coupling between adjacent manganese ions in the structure. Such impurities also have a pronounced effect on the value of the forbidden energy gap and on the electrical transport properties. This is well illustrated by the detailed study of iron-containing zinc sulfide by Keys et al. (1968). This study is of particular mineralogical interest because iron, by far the most important substituent in natural sphalerite, reaches concentrations of ≈20 atomic%. Measurements of the electrical conductivity of a sphalerite with 12.4 atomic% iron showed typical semiconductor behavior with a forbidden energy gap reduced to 0.49 eV. The absence of a measurable Hall effect and positive sign for the thermoelectric power suggested "hopping" of holes in a band of largely *d* orbital character as the conduction mechanism. The model requires the holes to be generated by the presence of Fe^{3+} ions (with one less *d* electron than Fe^{2+}) although only 1 in 800 iron atoms need be Fe^{3+}. Magnetic susceptibility measurements on the samples showed paramagnetic behavior at lower iron concentrations and a linear variation in susceptibility with iron content. At higher iron concentrations, the variation becomes non-linear and antiferromagnetic coupling is suggested (see Fig. 15). More recently, Nikolic et al. (1999) have studied the electronic transport properties of natural (Zn,Fe)S single crystals containing 12.2 wt% Fe and determined the mobility of (photogenerated) free carrier holes (μ_p) to be ~428 $cm^2\ V^{-1}\ s^{-1}$. Deulkar et al. (2003) studied the electrical properties of (Zn,Fe)S samples, performing resistivity and thermoelectric power measurements; the latter show *p*-type (semi)conductivity over a wide range of compositions. In this case, samples were prepared by sintering ZnS and FeS powders made by precipitation from aqueous solution

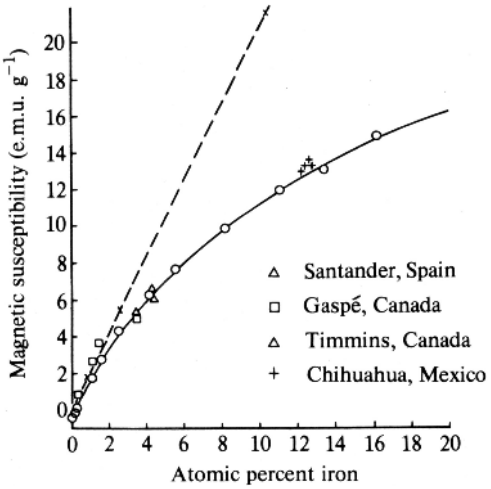

Figure 15. Magnetic susceptibility plotted against iron content for natural and synthetic (plotted as ○) iron-bearing sphalerites. In the dashed curve, the scale is expanded ten-fold; this shows the linear relationship between susceptibility and iron content at low temperatures. The diamagnetism due to ZnS has been subtracted from this curve. The solid curve shows the deviation from linear behavior at higher iron concentrations—the diamagnetic contribution of ZnS has not been subtracted in this case. After Keys et al. (1968).

which, although yielding a sphalerite structure solid solution single phase in most cases, at the highest concentrations produced some contamination by other phases (probably FeS). The sphalerite structure cadmium and mercury sulfides are also diamagnetic semiconductors, and there is an extensive literature on their electrical properties (Jellinek 1972). The CdS and HgS polymorphs probably also exhibit deviations from stoichiometry which can be linked with intrinsic semiconduction mechanisms.

***Chalcopyrite* (*$CuFeS_2$*).** In $CuFeS_2$, the zinc atoms of the sphalerite structure are replaced equally by copper and iron is antiferromagnetically ordered up to a Néel temperature of 823 K (Donnay et al. 1958; Teranishi 1961). The magnetic structure of chalcopyrite has been determined by neutron diffraction (Donnay et al. 1958) which shows that the spins on the two iron atoms, tetrahedrally bonded to a common sulfur atom, are opposed and directed along the *c*-axis. Chalcopyrite behaves as a typical semiconductor and exhibits intrinsic behavior above ~623 K (see Fig. 2) and extrinsic behavior below 223 K (Teranishi 1961), although as chalcopyrite is heated it loses sulfur with a consequent irreversible increase in conductivity (Frueh 1959). Room-temperature determinations on natural chalcopyrite nearly all show *n*-type conduction and band gap values of 0.5 eV, 0.33 eV and 0.6 eV are proposed by Austin et al. (1956), Baleshta and Dibbs (1969) and Teranishi et al. (1974). The metal enriched "stuffed" derivatives of chalcopyrite, talnakhite ($Cu_{18}Fe_{16}S_{32}$) and mooihoekite ($Cu_9Fe_9S_{16}$), have been studied by Townsend et al. (1971a). Talnakhite exhibits zero ferromagnetism and is antiferromagnetically ordered at room temperature, with a small paramagnetic component due to partial disorder. Mooihoekite shows weak ferromagnetism of approximately 0.2 μ_B/$Cu_sFe_9S_{16}$ formula unit (Townsend et al. 1971a).

***Stannite* (*Cu_2FeSnS_4*).** The antiferromagnetic coupling observed in chalcopyrite is no longer so readily possible in Cu_2FeSnS_4 because half of the iron atoms are replaced by tin. Stannite exhibits normal paramagnetic behavior in the temperature range 77–206 K (Eibschutz et al. 1967) and the susceptibility data indicate oxidation states of Cu_2^{2+} Fe^{2+} Sn^{4+} S_4^{2-}; a result confirmed by Mössbauer data. However, SQUID magnetometer measurements by Bernardini et al. (2000) of pure synthetic stannite show a transition to an antiferromagnetically ordered structure at 8 K (see Fig. 16). These authors also studied magnetic susceptibility as a function of temperature for iron-bearing samples of the stannite – kesterite (Cu_2ZnSnS_4) solid solution series, demonstrating paramagnetic (Curie-Weiss law) behavior attributed to the tetrahedrally coordinated Fe^{2+}, and determining Curie and Weiss constants. The isostructural mineral

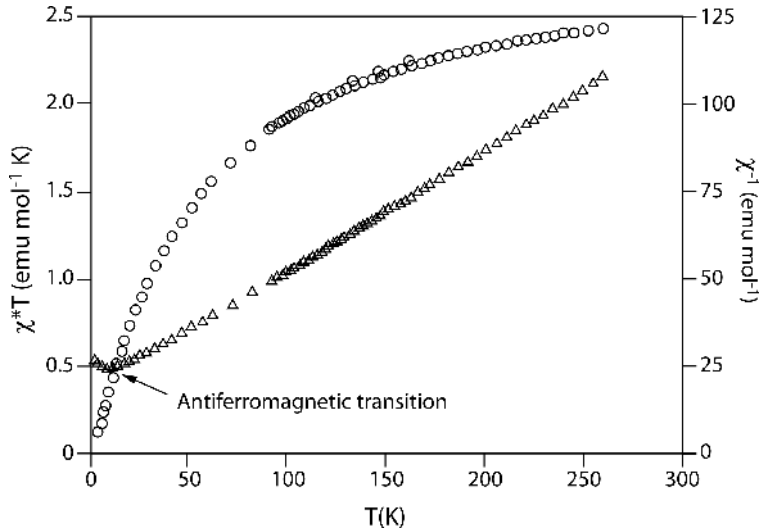

Figure 16. Graph to show X^{-1} vs. T (open triangle) and $X^{*}T$ *vs*. T (open circle) for synthetic stannite. After Bernardini et al. (2000). [Used with kind permission of Springer Science and Business Media]

briartite (Cu_2FeGeS_4) also exhibits a transition to an antiferromagnetically ordered mineral at very low temperature (T_N = 12 K) (Allemand and Wintenberger 1970).

***Cubanite* (*$CuFe_2S_3$*).** Cubanite is another mineral of this group which exhibits interesting magnetic and electrical properties; natural samples have been studied by Takeno et al. (1972). At room temperature, these authors, along with Sleight and Gillson (1973) observed semiconducting behavior in natural cubanite. Mössbauer data suggest formal valence states of $Cu^{+}(Fe^{2+}Fe^{3+})S_3$ in cubanite, but with electron hopping taking place between Fe^{2+} and Fe^{3+} ions across shared edges of the iron tetrahedra. Such hopping must be restricted to isolated pairs of iron atoms which must also be antiferromagnetically coupled to explain the ordered magnetism. However, weak ferromagnetism is exhibited by cubanite, and Fleet (1970) has suggested "canting" of the antiferromagnetic spins on the adjacent iron atoms as the origin; a mechanism similar to that suggested by Dzyaloshinsky (1958) to account for ferromagnetism in α-Fe_2O_3 which involves an imperfect antiparallel alignment of the spins.

Sulfides of pyrite (FeS_2) and related structure-types

The series of pyrite-structure disulfides from MnS_2 to ZnS_2 exhibits a wide range of electrical and magnetic properties as shown in Table 2. Hauerite (MnS_2) can be considered a "Class A" sulfide in terms of Jellinek's (1968) subdivisions. The localized *d* electrons of MnS_2 probably require excitation up into the σ^{*} band for conduction to occur. MnS_2 is cubic above the Néel temperature (295 K), and consists of an NaCl-like arrangement of Mn^{2+} and $(S_2)^{2-}$ ions, with the axes of the $(S_2)^{2-}$ groups directed along the various body diagonals of the cell. The magnetic data (Hastings et al. 1959) show that MnS_2 is paramagnetic and has five unpaired *d* electrons—a half-filled *d* shell which represents a particularly stable configuration. This sulfide undergoes a first-order phase transition from the paramagnetic phase to an antiferromagnetic phase at T_N = 48.2 K (Hastings and Corliss 1976). Chattopadhyay et al. (1991, 1995) investigated the magnetic diffuse scattering from neutron diffraction. They found that this first-order antiferromagnetic phase transition of MnS_2 could not be explained purely by symmetry considerations. The center of the diffuse scattering does not coincide with the commensurate superlattice point (1, ½, 0) but corresponds to an incommensurate

position $K = (1, k_y, 0)$, which is weakly temperature dependant (Fig. 17). This suggests that the antiferromagnetic phase transition in MnS_2 can be understood as a first-order lock-in transition from the incommensurate short-range order to the commensurate phase at T_N. Commensurate and incommensurate structures are represented schematically in Figure 18 (see also Makovicky 2006, this volume).

***Pyrite* (FeS_2).** FeS_2 is diamagnetic and must therefore have its six *d* electrons paired and completely filling the t_{2g} orbitals. The low-spin configuration of Fe^{2+} in pyrite is an indication of the strength of the ligand field due to the disulfide anions. Figure 19 shows a schematic band model for the pyrite-type disulfides (such qualitative MO/band-model energy level diagrams for pyrite-type disulfides are discussed in greater detail by Vaughan and Rosso (2006, this volume). Semiconducting properties are observed for pyrite in which the e_g^* levels are expected to overlap to form a band. The observed energy gap (≈0.9 eV) and large negative Seebeck

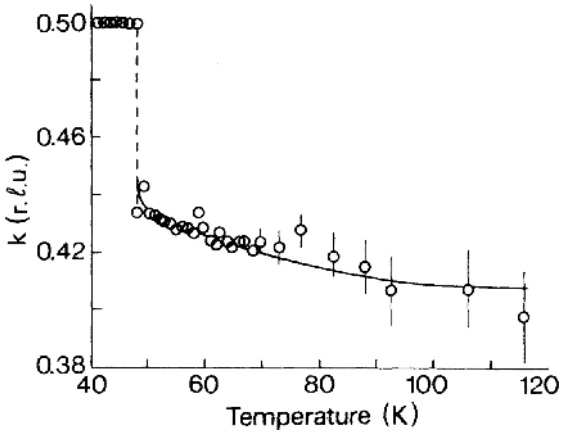

Figure 17. Temperature variation of the incommensurate component of the vector at which the diffuse magnetic neutron scattering is centered in MnS_2. [Reprinted with permission of American Physical Society, from Chattopadhyay et al. (1991), *Physical Review B*, Vol. 44, Fig. 5, p. 7396.]

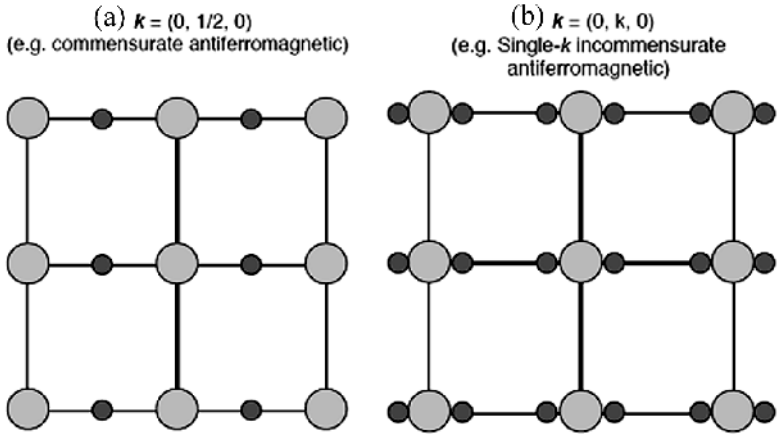

Figure 18. Schematic diagram of the relationship between nuclear (light grey) and magnetic (dark grey) diffraction peaks for (a) a commensurate antiferromagnet where the magnetic cell is a supercell of the nuclear structure and pure magnetic reflections appear as superlattice peaks in between the nuclear reflections, and (b) a single-*k* incommensurate antiferromagnet, where satellite peaks are present at position +*k* and –*k* from each nuclear reflection (Harrison 2006).

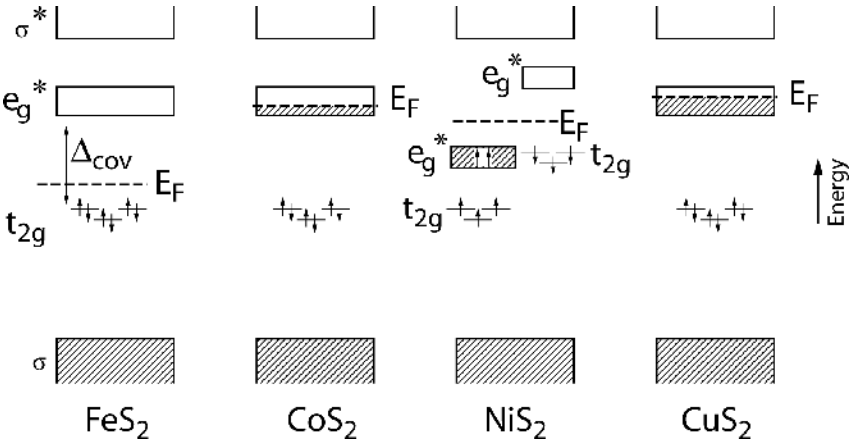

Figure 19. Schematic band-model energy level diagrams for the pyrite-type transition metal disulfides. E_F are the approximate Fermi levels; filled bands are shown shaded.

coefficient (Table 2) support a conduction process via electrons excited from the localized t_{2g} levels in the e_g^* band. Willeke et al. (1992) found that high purity single crystals prepared by chemical vapor transport are dominantly *n*-type conductors with carrier concentration (*n*) of 10^{16} cm^{-3} on the basis of Hall effect studies. Very similar results were obtained by Schieck et al. (1990) who also noted difficulties in synthesizing *p*-type single crystals. Harada (1998), who studied Hall effect along with conductivity and thermoelectric power of pure synthetic powder samples, showed that the sign of the dominant carriers in the intrinsic region is negative.

There has long been interest in reported deviations in the stoichiometry of pyrite from the ideal 1:2 ratio and its impact on properties. Birkholz et al. (1991) claimed from detailed X-ray diffraction measurements that synthetic pyrite can exhibit sulfur deficiency in the "few at% range." However, Ellmer and Hopfner (1997) undertook a detailed evaluation of all earlier work on the extent of pyrite nonstoichiometry and, combining this with theoretical arguments concerning the energetics of vacancy formation, concluded that deviations from the ideal stoichiometry do not exceed 1 at%. This would still be sufficient compositional variation to have a significant impact upon electrical properties. The considerable interest in the electrical properties of pyrite has arisen partly because of its possible use in photoelectrochemical and photovoltaic applications, particularly in solar cells. It is not our intention to discuss here the considerable literature dealing with this potential application, excellent reviews are provided elsewhere, for example, by Ennaoui and Tributsch (1984). One problem with using pyrite semiconductors in technical applications is the difficulty in obtaining high photopotentials with *n*-type or *p*-type material. The conductivity type can be adjusted by doping the crystals with P, As, Sb (*p*-type) or Co, Au, Cl, Br (*n*-type). High photo-effects are correlated with a low density of dislocations and low concentrations of impurities (Abd Al Halim et al. 2002). Ni-doped pyrite ($Fe_{0.99}Ni_{0.01}S_2$ – $Fe_{0.9}Ni_{0.1}S_2$) has been studied by Ho et al. (2004) and Ni shown to be an *n*-type dopant causing increasing conductivity with increasing concentration. Abd Al Halim et al. (2002) investigated the electrodeposition of Co and Cu on *n*-type pyrite slices. The free energy of interaction of a few monolayers of Co with pyrite was much higher than for the interaction of electrodeposited Cu with pyrite. This is because the Co atom was able to donate electrons into the conduction band of pyrite whereas the Cu atom is exchanging electrons with the valence band. The difference in free energy per electron corresponds to the width of the forbidden energy gap of pyrite (1 eV per electron). Not surprisingly, given the above findings, natural pyrite exhibits both *n*- and *p*-type semiconduction, sometimes within

the same single crystal. Figure 20 indicates the variation in the conductivity of pyrite and a review of compositional, textural and electrical variations in pyrite is provided in Abraitis et al. (2004). It has also been suggested that natural pyrite formed at lower temperatures tends to be *p*-type (iron-deficient) whereas high-temperature pyrite tends to be *n*-type (sulfur-deficient). Electron mobility in natural pyrite is highly variable (Fig. 4) but generally is about two orders of magnitude greater than hole mobility (Shuey 1975). As far as is known, marcasite exhibits a similar range of electrical and magnetic properties (Figs. 2 and 5).

***Cattierite* (CoS_2)** The magnetic data for cattierite (Table 2) indicate a *d* electron configuration of $(t_{2g})^6(e_g)^1$ and the metallic *n*-type conductivity observed supports conduction via the e_g^* band as shown in Figure 20. CoS_2 is very unusual amongst metal sulfides because it exhibits itinerant ferromagnetism below the Curie temperature of ~120 K, a phenomenon related to the very narrow e_g^* band width which also results in temperature-dependence of the paramagnetism above the Curie temperature. According to Adachi et al. (1969) the saturated magnetic moment for Co atoms in CoS_2 is $0.85\mu_B$. In the pyrite-cattierite solid solution $Fe_{1-x}S_2$-Co_xS_2, as Co is added, electrons occupy the previously empty e_g orbitals (in FeS_2) and, even with x values as low as 0.03, ferromagnetism is seen (Ramesha et al. 2004) although pure FeS_2 is a diamagnetic semiconductor.

Muro et al. (1996) undertook a detailed XMCD study of CoS_2 looking at both Co and S absorption edges. The Co 2*p* spectra and resulting XMCD are shown in Figure 21. The X-ray absorption spectrum (XAS) shows the Co $2p_{3/2}$ and $2p_{1/2}$ absorption peaks and the difference between the reversed magnetization directions is clear. The XMCD spectrum shows a positive peak corresponding to the $2p_{3/2}$ XAS and a negative peak at the $2p_{1/2}$ peak with the change

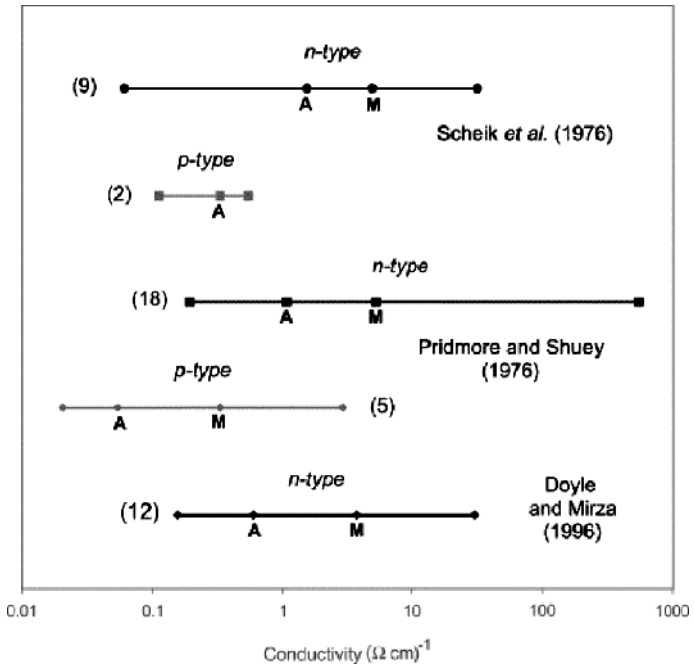

Figure 20. Variations in the conductivities of pyrite, based on the work of Doyle and Mirza (1996), Pridmore and Shuey (1976) and Schieck et al. (1990). Note the logarithmic conductivity scale. Maximum and minimum values are shown in each case. (A denotes the mean value, M denotes the median and the bracketed Figure nest to each bar denotes the number of measurements).

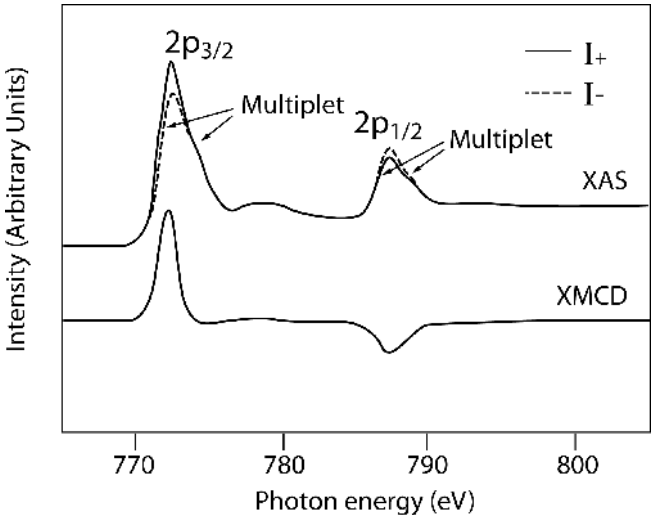

Figure 21. Co $L_{3,2}$ XAS absorption and XMCD spectra of synthetic CoS_2. The absorption spectra for the two magnetization directions are shown, with the XMCD difference spectra - XMCD intensity enhanced by a factor of three. [Used with permission of S. Suga and the American Physical Society, from Muro et al. (1996), *Physcial Review B,* Vol. 53, Fig. 2b, p. 7057.]

in sign across the two edges due to the different effect on the spin up/spin down electrons. Multiplet structure is observed in the main absorption peaks (indicated in Fig. 21) and the resulting XMCD is dependent on the individual multiplet components; in this case, the main contribution comes from the multiplet on the lower energy side of the main XAS peaks with a decrease in XMCD on the high energy side of the $2p_{3/2}$ peak. This dependence reveals the importance of the electron-core hole exchange and Coulomb interactions for the Co $2p - 3d$ excitation. Using the sum rules and the XMCD spectrum, the integrated intensity ratio of the Co $2p_{3/2}$ and $2p_{1/2}$ is 1.5:1.0 and the orbital magnetic moment, $\langle L_z \rangle$, is evaluated as $0.060\mu_B$ and the $\langle L_z \rangle / \langle S_z \rangle$ is 0.18 ($\langle S_z \rangle$ is the spin magnetic moment). The high orbital moment (>10% of the total moment) suggests localized 3d orbitals and the presence of multiplet structure in the spectrum supports localization. There are also satellite peaks 6 eV above the XAS and XMCD main peaks which are due to hybridization of the Co 3*d* and S states and Muro et al. (1996) also recorded the XMCD spectrum from the S 2*p* XAS. This confirms the S 2*p* hybridization with the Co 3*d* state and, therefore, a slight magnetic moment on the S atom. As a result of these magnetic properties, CoS_2 has potential use in the rapidly developing area of spintronics (Néel and Benoit 1953; Jarrett et al. 1968; Muro et al. 1996; Ramesha et al. 2004).

The magnetic properties of CoS_2 have also been examined using neutron diffraction by a number of groups (Ohsawa et al. 1976a, 1976b; Panissod et al. 1979; Brown et al. 2005). Panissod et al. (1979) used neutron diffraction in conjunction with NMR in their study of the $CoS_{2-x}Se_x$ solid solution which indicated that the magnetic properties are determined by an inhomogeneous distribution of moments on Co atoms. The neutron diffraction spectra contained overlapping magnetic components and nuclear components below the T_C of 120 K (Fig. 22). The NMR data confirm the presence of both ferromagnetic and paramagnetic Co atoms in $CoS_{2-x}Se_x$ with the appearance of the non-magnetic atoms relating to Se in the inner coordination sphere. This can be explained by the narrower band width of the antibonding 3*p*-states of S in CoS_2 than the 4*p*-states of Se in $CoSe_2$ (Yamada et al. 1998). The moment on the magnetic Co atoms was determined as $0.9\mu_B$, as in pure CoS_2 and at values $x < 0.28$

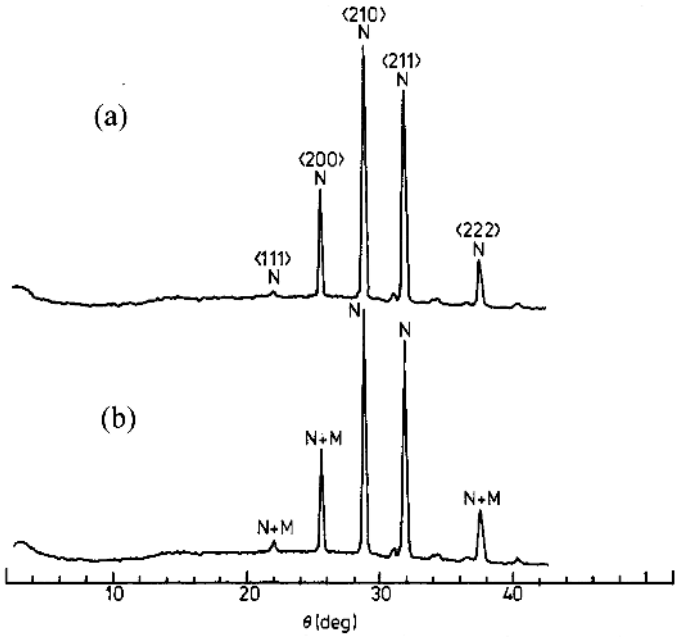

Figure 22. Neutron diffraction patterns ($2 \leq \theta \leq 52°$) for $CoS_{1.675}Se_{0.325}$ at 140 K (a) and 4 K (b) [Used with permission of IOP Publishing Limited, from Panissod et al. (1979).]

in $CoS_{2-x}Se_x$, almost all Co atoms are ferromagnetic. Polarized neutron diffraction has also revealed a small magnetic moment distributed around S atoms in CoS_2. The magnetic moment distribution is aspherical around the Co nuclei and results from a covalent bonding effect between $3d_{eg}$ orbitals of Co atoms and $3p\pi$ orbitals of S atoms (Ohsawa et al. 1976b).

Investigating the possibility that CoS_2 is a half-metallic ferromagnet, Brown et al. (2005) used unpolarised neutrons on a single crystal to define the crystal structure, atomic positions and a magnetic moment per cobalt atom of $0.882\mu_B$ at a temperature of 20 K. Using a 9.6 T applied field, the flipping ratio was determined for reflections of the ferromagnetic phase at 1.8 K and the paramagnetic phase at 150 K. The magnetization associated with the Co atoms in full cubic symmetry (h,k,l = all odd or all even) coincide and contribute to the crystal lattice reflections, while those associated with mixed index reflections are either magnetic in origin and associated with the non-cubic Co atoms or with the S atoms. The orbital contribution to the moment was 15% at 150 K, but was small at 1.8 K and 300 K, a factor of two less than that determined from XMCD measurements. The data suggest that the magnetization distribution around the Co^{2+} ions in the ferromagnetic phase at 1.8 K is nearly spherical as a result of e_g, t_{2g} mixing, with a small magnetic moment of approximately 2% of that on the Co atoms residing on the S atoms. At 150 K, just above the T_c the ordered paramagnetism has the aspericity characteristics of e_g electrons. At higher temperatures (300 K), the band with the highest density of states lies sufficiently close to the Fermi energy for thermal excitations to create holes in it, resulting in orbitals with t_{2g} character contributing more to the magnetization. The magnetization distribution observed in CoS_2 indicates that, in the ferromagnetic phase, both e_g and t_{2g} bands contain unpaired electrons. Therefore, CoS_2 is not a half-metallic ferromagnet (Brown et al. 2005).

***Vaesite* (NiS_2).** This mineral exhibits unusual properties as a result of unpaired *d* electrons which result in the splitting of the t_{2g} and e_g^* energy levels into two sets containing electrons

of opposite spin, *spin-up* and *spin-down* (Fig. 19). NiS_2 is a Mott-Hubbard semiconductor because the splitting is greater than the width of the e_g^* band and the resulting band gap (~0.27 eV at 300 K) (Kautz et al. 1972) is the energy required to excite an electron into the empty *spin-down* e_g^* band. The insulating ground state is only present when there is no vacancy on the Ni sites and disappears progressively with the introduction of vacancies or the substitution of S by Se to form a metallic phase (Adachi et al. 1969). These metal-insulator transitions of the Mott-Hubbard type play a fundamental role in the physical transformation of the 3*d* electronic states from localized atomic states on the insulating side into itinerant band states on the metallic side; no intermediate state is possible. Magnetic ordering effects in NiS_2 have been repeatedly investigated though magnetization and neutron diffraction studies. Neutron diffraction showed that magnetic ordering occurs in two steps: (1) a transition to the antiferromagnetic state takes place (40-60 K), with the Néel point depending on the stoichiometry, and (2) a second transition at 30 K to a weak ferromagnetic state which coexists with the first state. The magnetic moments in the two configurations are 1.0 and $0.6\mu_B$ respectively (Honig and Spalek 1998).

CuS_2 and ZnS_2. The transition metal disulfides CuS_2 and ZnS_2 can be synthesized at high pressures but are not found in nature. In CuS_2 (d^9), the e_g^* band results in temperature-independent Pauli paramagnetism. This material is an example of "class D" compound of Jellinek (1968). Electrical resistivity data $\rho(T)$ for CuS_2 show a metallic behavior which is consistent with band-structure calculations. The Hall coefficient is weakly temperature dependant and positive, implying that the charge carriers and, therefore, the magnetic properties, are dominated by holes in the anion *p* band (Ueda et al. 2002). Krill et al. (1976) found a high *p* and *d* density of states at the Fermi level which is indicative of a relatively narrow conduction band. A sudden decrease of the bulk susceptibility was observed below 160 K. In ZnS_2, the *d* levels are completely filled with electrons so that the material is no longer a transition metal sulfide. Properties akin to ZnS are observed; i.e., it is a diamagnetic semiconductor with a large band gap.

Sulfides with halite (NaCl) structures

Galena (PbS). PbS is a diamagnetic semiconductor, the properties of which have been reviewed by Dalven (1969). The forbidden energy gap at 300 K is 0.41 eV and values for the isostructural PbSe (clausthalite) and PbTe (altaite) of 0.27 and 0.31 eV have been reported (Zemel et al. 1965). Figure 1b is a simplistic representation of the type of band structure found in galena, although a great deal more detailed information is actually known about the band structure of PbS (Vaughan and Rosso 2006, this volume). The conduction mechanisms and carrier concentrations, as in all such compounds, are very sensitive to precise stoichiometry. Slightly metal-rich galenas with *n*-type semiconductivity or sulfur-rich *p*-type semiconductors are readily synthesized. Most natural galena samples exhibit *n*-type conductivity, although carrier concentrations are strongly influenced by the presence of silver, bismuth and antimony in the samples (Kravchenko et al. 1966). Shuey (1975) observed that galena exhibiting *p*-type conductivity occurs particularly from limestone-lead-zinc ("Mississippi Valley type") mineral deposits and silver-rich hydrothermal deposits. Conductivities and transport phenomena in synthetic samples are discussed by Dalven (1969). Conductivities range over several orders of magnitude. The plot of hole mobility against reciprocal temperature in Figure 4 is for a synthetic *p*-type galena, although other *n*- and *p*-type galenas exhibit similar behavior over this temperature range. Nimtz and Schlicht (1983) studied a series of narrow-gap semiconductors based on PbS over a range of temperatures and pressures, including Sn-bearing sulfides, selenides and tellurides. In particular, optical properties, band structures and transport properties were investigated.

Alabandite (α-MnS). This sulfide actually exists in three crystalline modifications, the halite structure (alabandite, α-MnS) and the sphlalerite and wurzite structures, but α-MnS is the

most stable form. Neutron diffraction measurements indicate that, below its Néel temperature (150 K), α-MnS is a high spin antiferromagnet (Corliss et al. 1956). Experimentally, Mn moments of $\mu = 4.54\mu_B$ have been reported. According to the Hall measurements, the conductivity in α-MnS is a result of holes in the 3*d* band of the manganese ions (Aplesnin et al. 2004), with a hole concentration per Mn ion of $n \sim 0.1$ at $T = 435$ K (Aplesnin et al. 2005).

The electronic structure of α-MnS has been studied by Tappero and Lichanot (1998), Tappero et al. (2001) and Youn et al. (2004), using quantum mechanical calculations and it provides an example of the differences between various electronic structure models. Tappero and Lichanot (1998) showed that the predicted electronic structure of α-MnS is quite different when calculated using a Hartree-Fock (HF) compared to a Density Functional Theory (DFT) formalism (see Vaughan and Rosso 2006, this volume). In the HF scheme, α-MnS is a highly ionic compound with a magnetic moment per Mn^{2+} of $4.90\mu_B$ corresponding to a high spin electronic configuration $t_{2g}^3 e_g^2$. It has strong insulator character as shown by the band structure. Using DFT, α-MnS is a less ionic compound, the Mn *d* shell is populated with spin down electrons and the magnetic moment is $4.40\mu_B$. Comparisons with the experimental data ($\mu = 4.54\mu_B$) indicate that the DFT scheme gives a better description of the electronic structure of α-MnS. However, recent simulations of the neutron diffraction spectra of α-MnS have shown that the use of the exact HF exchange potential is more suitable for an accurate determination of electron charge and spin densities (Tappero et al. 2001). Youn et al. (2004) applied local density approximation band calculations, where the strong Mn *d* correlation effect is taken into consideration, to obtain an enhanced energy gap and magnetic moment for α-MnS, more comparable with the experimental data. α-MnS is a band insulator even though correlation effect between the *d* electrons is large, and can be considered as a "crossroads" material between a charge transfer and a band insulator.

MnS can also be doped with other transition metal (*TM*) ions to form the disordered system of $Mn_{1-x}TM_xS$ (*TM* = Cr, Fe, V) in which metal-insulator transitions, connected with electron localization at the edge of the conduction band have been observed. The disordered solid solutions form two antiferromagnetic 3*d* metal monosulfides at intermediate compositions, exhibiting magnetic properties different from the original MnS (Petrakovskii et al. 1995). The diluted magnetic semiconductor $Mn_{1-x}Fe_xS$ exhibits colossal magnetoresistance, i.e., a strong resistivity decrease in an applied magnetic field.

Rare earth sulfides. A number of the rare-earth sulfides, including europium, gadolinium and lanthanum sulfide, have simple NaCl structures. They are magnetic semiconductors, exhibiting pure spin magnetism with magnetic ordering varying from ferromagnetic (EuS) to antiferromagnetic (GaS) and diamagnetic (LaS) (Hauger et al. 1976; Klein et al. 1976). These sulfides have potential applications in electroluminescent devices as a result of their electro-optical characteristics.

Sulfides with niccolite (NiAs)-based structures

The pyrrhotites are metal-deficient iron monosulfides, $Fe_{1-x}S$, and form a structurally complex series between monoclinic Fe_7S_8 and hexagonal FeS (Makovicky 2006, this volume). Troilite is the low temperature (<140 °C) stoichiometric form of FeS. The pyrrhotites are based on the NiAs-type structure, and their ferri- and antiferromagnetic magnetic properties have been of particular interest to mineralogists, geologists and mineral technologists.

Troilite (FeS). This has alternating Fe and S layers parallel to 001 with all the metal sites filled. The magnetic properties of FeS have been studied by a number of authors (Haraldsen 1941a, 1941b; Benoit 1952; Murakami and Hirahara 1958; Schwarz and Vaughan 1972; Kruse 1990; Li and Franzen 1996; Li et al. 1996). The change in magnetization of troilite during heating is shown in Figure 23a and indicates that above the so-called "β-transition" paramagnetic behavior is observed. An effective magnetic moment of $5.24\ \mu_B$ has been

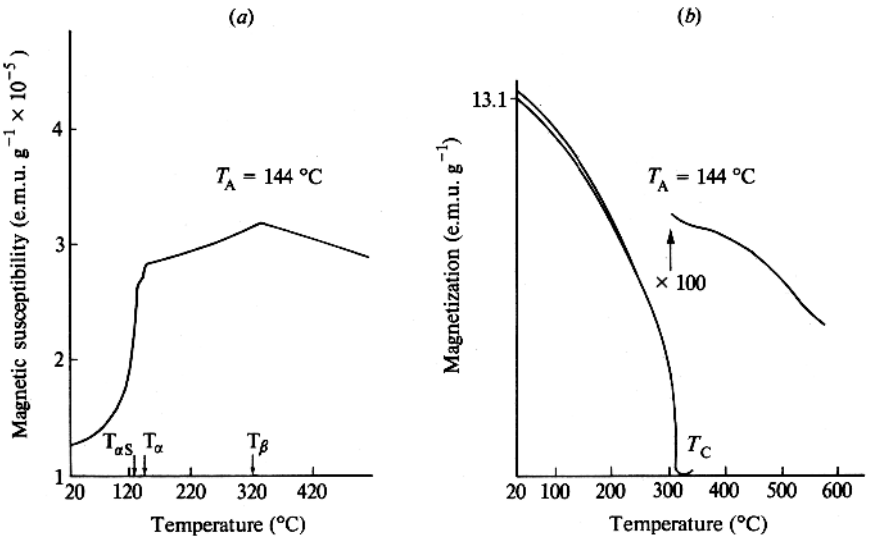

Figure 23. Thermomagnetic curves showing the thermal change in susceptibility or magnetization (J, applied field, 5350 Oe) for: (a) troilite and (b) monoclinic pyrrhotite; T_A is annealing temperature of synthetic sample, T_α, T_β and $T_{\alpha S}$ are transition temperatures and T_c is the Curie temperature. After Schwarz and Vaughan (1972).

reported from high-temperature susceptibility measurements. The β-transition, which extends to metal-deficient compositions but still occurs at ~315 °C, has been attributed by some authors to a first-order crystallographic transformation. However, Hirone et al. (1954) attribute the β-transition to the Néel temperature over the whole range of troilite–pyrrhotite compositions, a theory supported by specific heat measurements in this temperature range which agree with predicted values for such a mechanism. In FeS, below T_β, antiferromagnetic behavior is observed, but two further transitions occur. The α-transition represents the change from the high-temperature NiAs structure to the troilite superstructure. The second transition, in some reports occurring at the same temperature as T_α (140 °C), is attributed to a change in orientation of the antiferromagnetically ordered spins. This "Morin transition" (at temperature $T_{\alpha s}$) is associated with the structural transformation at T_α and has been studied by neutron diffraction and Mössbauer spectroscopy (Andresen and Torbo 1967). In an X-ray diffraction and Mössbauer study of phase transitions in synthetic FeS and the associated kinetics, Kruse (1990) found that the α-transition is spread over ~40 °C but is complete at 140 °C and the transition involving a change in spin orientation is completed by 159 °C in these synthetic samples. However, the later effect was not complete at 156 °C after 23 days when troilite from a meteorite was used.

Determination of its electrical properties shows that troilite is a semiconductor which exhibits considerable electrical anisotropy and a sharp change in c-axis conductivity at T_α (Hirahara and Murakami 1958). Townsend et al. (1976) have observed a semiconductor-metal transition in FeS at T_α from electrical, magnetic and Mössbauer measurements on single crystals. A semiconductor-metal transition has also been observed by Kobayashi et al. (2005) at high pressure (2.9 GPa) and low temperature (100 K). Troilite (i.e., FeS below T_α) is a ferroelectric material, a property observed and discussed by van den Berg et al. (1969).

***Pyrrhotite* (Fe_7S_8).** The Fe_7S_8 endmember has a monoclinic "defect" NiAs structure, in which cation-deficient layers alternate with fully occupied cation layers. The vacancies are

in alternate sites, in every other row of cations in the layer, and the ABCD stacking of the vacancy layers leads to a 4C notation for the classic pyrrhotite structure. Increased iron in the structure filling the vacancies ($Fe_{7+x}S_8$) leads to less regular metal ordering in the layers and more complex stacking of the metal deficient layers and most commonly a hexagonal symmetry (Lotgering 1956; Makovicky 2006, this volume).

Monoclinic pyrrhotite is a very highly conducting material (see Fig. 2), although there appears to be some dispute regarding the actual mechanism of the conductivity. Synthetic samples show a room-temperature resistivity of $\approx 3 \times 10^{-4}\,\Omega$cm which increases with decreasing temperature as in semiconductors, whereas natural samples exhibit a temperature dependence characteristic of metals. Theodossiou (1965) made resistivity and Hall effect measurements on natural samples; *p*-type conduction was observed both normal and parallel to the *c*-axis direction at room temperature (although *n*-type conduction was found perpendicular to the *c*-axis below −108 °C). Synthetic hexagonal pyrrhotite has a room-temperature resistivity of ~10^{-2}–10^{-3} Ω cm (Perthel 1960) and thermoelectric power measurements indicate *p*-type conduction below 225 °C and *n*-type above this temperature (Kamigaichi 1956). Method of preparation strongly influences the electrical, magnetic and structural properties of these "intermediate" pyrrhotites.

The magnetic properties of pyrrhotites with compositions between FeS and Fe_7S_8 ($Fe_{0.875}S$) can best be visualized with reference to the magnetic phase diagram shown in Figure 24. Here, synthesized initial compositions (annealed at 144 °C) are plotted along the abscissa, and the ordinate combines a temperature scale and a susceptibility/magnetization scale. Solid lines on the diagram are magnetic phase transitions with reference to the temperature scale, and dashed lines represent susceptibility in the region where antiferromagnetic behavior is observed. Dotted lines occur in the ferromagnetic region of the diagram and represent the estimated saturation

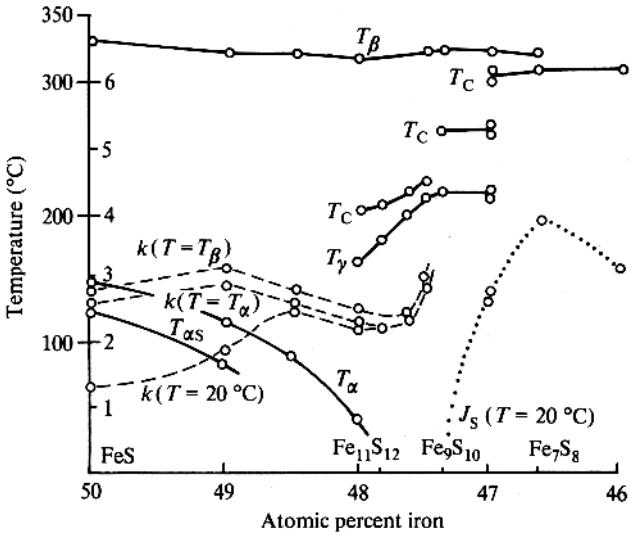

Figure 24. Magnetic phase diagram for synthetic pyrrhotite samples annealed at 144 °C. Initial compositions are plotted along the abscissa and the ordinate combines a temperature/magnetization scale. The solid lines are magnetic phase transitions with reference to the temperature scale and the dashed lines represent susceptibility in the region where antiferromagnetic behavior is observed (scale of $k \times 10^5$ emu g^{-1}). The dotted line appears in the ferromagnetic region and represents the estimated saturation magnetization J_s (on this scale $J_s \times 1/5$ emu g^{-1}) at 20 °C. The susceptibility is recorded at 20 °C and at the β-transition and α-transition temperatures. After Schwarz and Vaughan (1972).

magnetization (J_s). Susceptibility and saturation magnetization are shown at 20 °C and at the α- and β-transition temperatures. Compositions containing ≥48 at% iron ($Fe_{0.92}S$) exhibit antiferromagnetic behavior. The origins of the β-transition, α-transition and Morin transition ($T_{\alpha s}$) are as discussed for troilite, although with increasing metal deficiency the α-transition corresponds to the solvus between the "troilite + hexagonal pyrrhotite" two-phase field and the hexagonal pyrrhotite field. The region of 48.0 to 47.0 at% iron (~$Fe_{0.92}S$ to $Fe_{0.89}S$) (containing the "intermediate" or "low-temperature hexagonal" pyrrhotites) is of particular interest. Such compositions, at the so called γ-transition or anti-Curie point of Haraldsen (1941a,b), exhibit a very sharp increase in susceptibility which is retained over only a short temperature range (see Fig. 24). This apparent ferrimagnetism disappears at a "Curie temperature" well below T_β. At compositions <47 at% Fe, the pyrrhotite is ferrimagnetic (note that Fe_7S_8 contains 46.67 at% Fe). Thermomagnetic curves for natural monoclinic pyrrhotite (Fig. 23b) show characteristic behavior, i.e., initially high magnetization which gradually decreases on heating to the Curie temperature (315 ºC).

Various theories of both vacancy and spin order = disorder transitions have been put forward to explain the magnetization in pyrrhotites (Hirone et al. 1954; Lotgering 1956; Kawiaminami and Okazaki 1970; Ward 1970; Schwarz and Vaughan 1972). According to Néel (1953), the spontaneous room temperature ferrimagnetic behavior of monoclinic pyrrhotite is due to the ferrimagnetic alignment of cations (Fe) within layers, with an antiparallel arrangement of the spins on the iron atoms on successive cation layers in the (001) plane (Bertaut 1953). There is antiferromagnetic coupling between layers and, as there are uncompensated magnetic moments, this results in the ferrimagnetic behavior. Kruse (1990) undertook a Mössbauer investigation of hexagonal pyrrhotites and noted that repulsion may inhibit the development of monoclinic pyrrhotite at room temperature. Marusak and Mulay (1980, 1979) used data from X-ray diffraction, magnetic and Mössbauer studies, and arguments based on reaction rate theory, to support a vacancy ordering model. Here, the observed ferrimagnetism above the gamma transition (Fig. 24) is attributed to a vacancy-ordered 4C superstructure and the antiferromagnetism below it to a different (5C) superstructure (Fleet 2006, this volume; Makovicky 2006, this volume). Novakova and Gendler (1995) also used Mössbauer spectroscopy to observe hexagonal and monoclinic nonstoichiometric pyrrhotites with varied degrees of vacancy ordering and disordering during pyrite oxidation.

Li and Franzen (1996) and Li et al. (1996) undertook a detailed thermometric study of the structural and magnetic transitions in the "$Fe_{0.875}S$ – FeS" series (Fe_7S_8, pyrrhotite – $Fe_{1.0}S$, troilite). They confirmed the previous structural changes, noting also a transformation in Fe_7S_8 to a trigonal 3C stacking between 200-240 °C and, in the range of $Fe_{0.88}S$ to $Fe_{0.92}S$ a magnetic "λ-transition" takes place with an increase and then decrease in magnetization over the range 200-250 °C, consistent with the anti-Curie point behavior recorded by Haraldsen (see above). A large enthalpy change at 315 °C determined using differential thermal analysis (DTA) of Fe_7S_8 is coincident with the magnetic transition and is associated with the disordering of the vacancies and offers further confirmation that this is the Curie temperature of monoclinic Fe_7S_8 (Li and Franzen 1996; Li et al. 1996).

A very detailed, time of flight powder neutron diffraction study of synthetic Fe_7S_8 in the temperature range 11-773 K by Powell et al. (2004) further confirmed the existing magnetic models. The powder diffraction data produced (Fig. 25) fitted well with the assumed monoclinic unit cell, but there were major discrepancies between calculated and observed intensities, especially the strongest reflection at 5.689 Å. Although this represents $(001)_{NiAs}$ there is no calculated reflection at this angle of 2θ and this is also the case for reflections at 2.62 Å. These additional reflections/intensities are magnetic in origin and coincident with the potential structural reflections. Thermometric studies revealed the $(001)_{NiAs}$ magnetic reflection decreases with increasing temperature and disappears at 325 °C, with little hysteresis

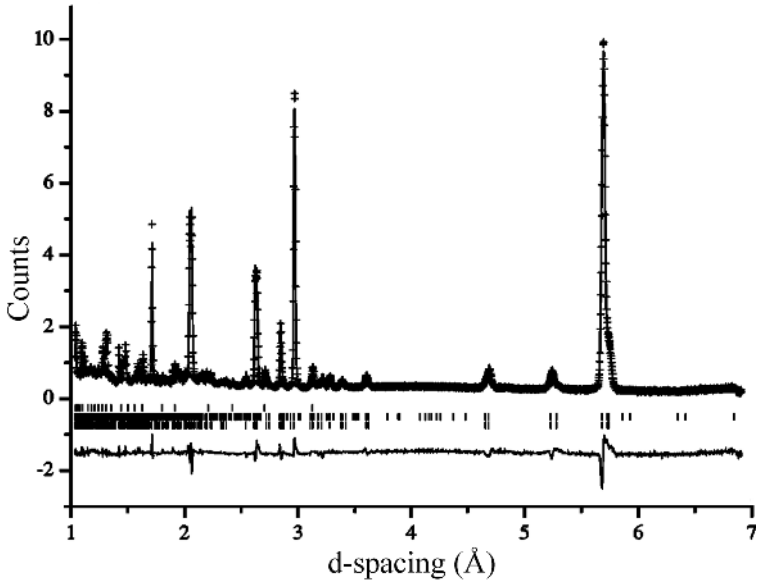

Figure 25. Final observed (crosses), calculated (full line) and difference (lower full line) neutron profiles for Fe_7S_8 collected at 11 K. [Used with permission of A. Powell and the American Physical Society, from Powell et al. (2004), *Physical Review B,* Vol. 70, Fig. 2, p. 014415-3.]

on cooling (Fig. 26). This disappearance is coincident with the loss of the monoclinic 4C structure and the formation of a hexagonal, cation-deficient NiAs structure, in which the vacancies are statistically distributed between all the layers, demonstrating the link between magnetic and structural properties. The ordered magnetic moment was measured as $3.16\mu_B$ at 11 K and $2.993\mu_B$ at 298 K.

An XMCD study of monoclinic (4C) pyrrhotite was recently carried out by Pearce et al. (2006a). The results have not yet been analysed in terms of the absolute magnetic moments for the individual atoms but the XMCD spectrum, produced due to the net magnetic moments in the cation deficient layers, is shown in Figure 27.

A SQUID study of selenium-bearing pyrrhotites (Ericsson et al. 2004, 1997) revealed a spin-flip transition due to the re-orientation of the spins from perpendicular (parallel to *a*,*b*) to parallel to the c axis that is not present in S-rich members of the Fe_7S_8-Fe_7Se_8 series. By varying the applied fields the relationship between composition and vacancy ordering was established with superstructures (of 3C and 4C) close to the end-member compositions ($y < 0.15$; $0.85 < y$ in $Fe_7(S_{1-y}Se_y)_8$. Figure 28 shows the magnetization versus applied field curves measured at 150 K for four different compositions that illustrate the different types of behavior. The transition temperature is lowered below the 130 K found in Fe_7Se_8 with increasing S-content.

CoS and NiS. The cobalt and nickel monosulfides with the NiAs-type structure can be metastably retained on quenching from high temperature and have been studied to determine their magnetic and electrical properties. CoS is antiferromagnetically ordered with $T_N = 358$ K; the effective magnetic moment on the cobalt atom is $1.7\mu_B$ (Benoit 1955). Metallic conductivity has been reported. NiS is extremely interesting; Sparks and Komoto (1968) observed a phase transition from a low-temperature antiferromagnetic semiconductor to a paramagnetic metallic phase at close to room temperature ($T_N \approx 263$ K). This transition temperature is strongly dependent on the sulfur content (NiS – $NiS_{1.03}$ is the approximate range of compositions) and

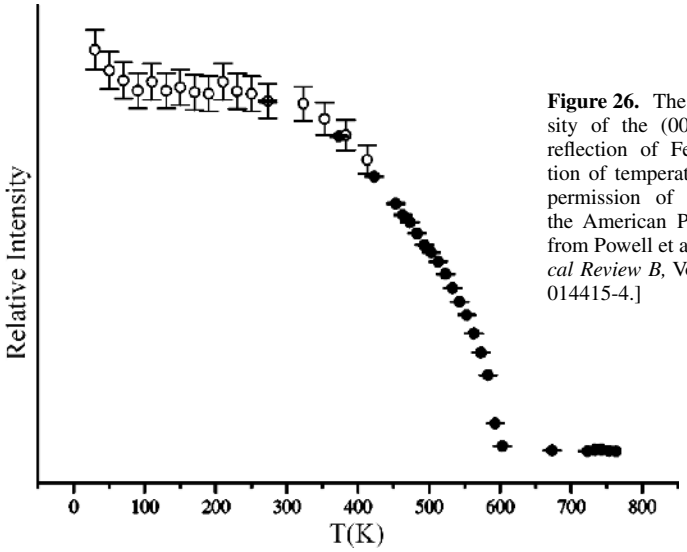

Figure 26. The relative intensity of the $(001)_{NiAs}$ magnetic reflection of Fe_7S_8 as a function of temperature. [Used with permission of A. Powell and the American Physical Society, from Powell et al. (2004), *Physical Review B,* Vol. 70, Fig. 4, p. 014415-4.]

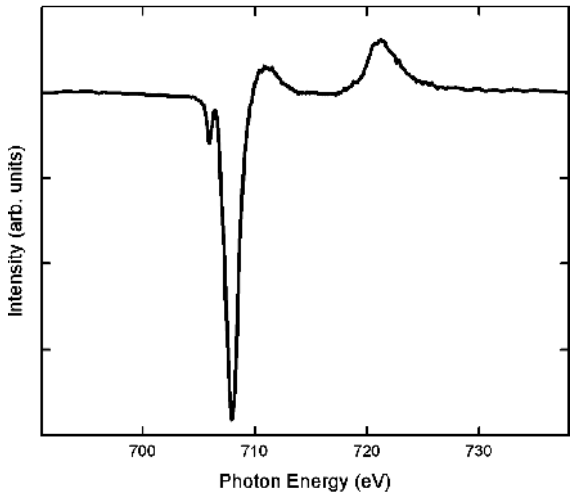

Figure 27. XMCD spectrum of natural pyrrhotite. The spectrum was collected in a reversible 0.6 Tesla magnetic field (Pearce et al. 2006a).

detailed electrical, magnetic and Mössbauer studies of this transition have been performed (Townsend et al. 1971b; Coey and Brusetti 1975). The low-temperature form of NiS (millerite) is reported to be metallic and Pauli paramagnetic (Hulliger 1968), properties attributed to the metal-metal bonding which stabilizes this structure (Grice and Ferguson 1974; Rajamani and Prewitt 1974; Vaughan and Rosso 2006, this volume). McCammon and Price (1982) have studied the magnetic behavior of $(Fe,Co)S_{1-x}$ solid solutions using Mossbauer spectroscopy; samples with >16% Fe show magnetic ordering but, below that concentration, no ordering is observed down to 4.2 K. The absence of magnetic ordering at the lower Fe concentrations is attributed to a substantial increase in electron delocalization towards the ligands as the M-S distance decreases, rather than a high-spin to low spin transition which is ruled out by the Mossbauer (isomer shift) parameters.

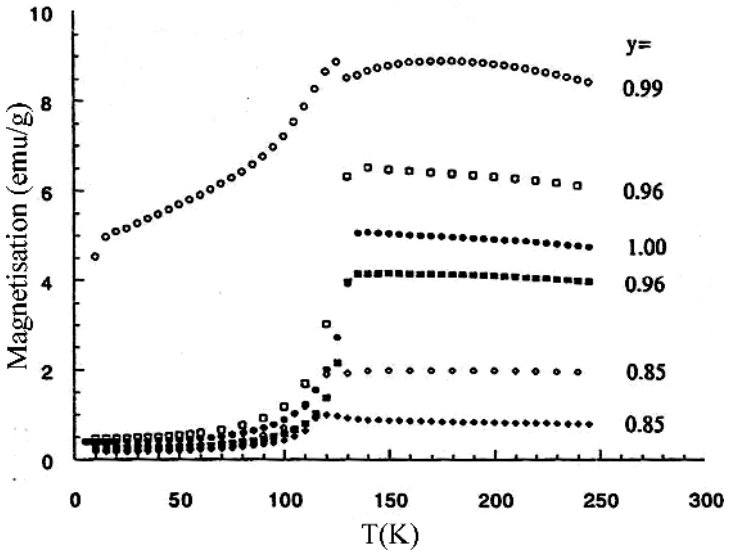

Figure 28. Magnetization measured at increasing temperatures in an external field of 1 kOe for zero field cooled $Fe_7(S_{1-y}Se_y)_8$ samples. The abrupt change in magnetization taking place at 130 K in Fe_7Se_8 is due to a spin-flip. Open symbols indicate samples annealed at 423 K; filled symbols indicate samples annealed at 873 K. [Used by permission of E. Schweizerbart'sche Verlagsbuchhandlung <http://www.schweizerbart.de>, from Ericsson et al. (1997), Eur. J. Mineral. Vol. 9, p. 1131-1146.] (Ericsson et al. 1997).

Mackinawite, smythite, greigite and other thiospinels

Three other iron sulfide minerals should be mentioned because of their geochemical importance or potential relevance to magnetic studies. The tetragonal iron monosulfide, mackinawite (FeS) is the first formed sulfide in many modern sedimentary environments; a range of transformations of this mineral can occur, leading ultimately to pyrite or pyrrhotite (Fleet 2006, this volume; Rickard and Luther 2006, this volume), but in some cases involving greigite (Fe_3S_4). The apparently much rarer mineral smythite (probable composition ~Fe_9S_{11}), like the other two phases, appears only to occur in very low temperature hydrothermal (Krupp 1994) or sedimentary environments. These minerals only occur as fine particles and cannot be synthesized except via precipitation from aqueous solution. Mackinawite has a layer structure, greigite has a spinel structure (as the sulfide analog of magnetite) and smythite appears to be structurally related to pyrrhotite but with an even higher concentration of vacant sites than is found in monoclinic pyrrhotite (Makovicky 2006, this volume).

The lack of single crystal material for all of these phases, and the metastable nature of mackinawite and greigite, in particular, has limited attempts to define their electrical and magnetic properties. From their structures and compositions, all three are assumed to be highly conducting (although a mackinawite crystal might be expected to show lower conductivity normal to the layers in its structure). Unlike electrical properties, magnetic properties can be measured in bulk, and inferences drawn from techniques such as Mössbauer spectroscopy (Wincott and Vaughan 2006, this volume). Mackinawite shows no magnetic ordering down to very low temperatures (<4.2 K) and is believed to be a Pauli paramagnet. Both greigite and smythite show evidence of being magnetically ordered up to (and probably above) room temperature. The Curie temperature of synthetic greigite has been reported at between 297 and 527 °C based on various extrapolations, but several authors urge caution over such data as greigite probably

begins to break down at ~200 °C (Roberts 1995; Snowball and Torii 1999). Smythite has a net magnetic moment and Mössbauer parameters in line with the kind of ferrimagnetism seen in monoclinic pyrrhotite (Hoffmann 1993). Greigite is also regarded as a ferrimagnet, with this behavior arising in the same way as for magnetite (Fe_3O_4), although the saturation magnetization per formula unit is 2.5× less than Fe_3O_4 and it shows no Verwey transition. An XMCD study of greigite indicated the presence of iron vancancies in both natural and synthetic Fe_3S_4 leading to a structure similar to that for the lacunary iron oxide maghemite γ-Fe_2O_3 (Letard et al. 2005).

Such departures from stoichiometry have been found to affect the magnetic and transport properties in a range of thiospinels. In the semiconducting and ferromagnetic chromium chalcogenide spinels ($A^{2+}Cr^{3+}{}_2S_4$), such as $CdCr_2S_4$, $CoCr_2S_4$ and $FeCr_2S_4$, the defects appear as sulfur vacancies, affecting the Curie point and the saturation magnetization. The type of conduction (*n*-type or *p*-type) depends on the nature of the defects and the ion in the spinel lattice (Gibart et al. 1976). Natural and synthetic thiospinels of the series polydymite (Ni_3S_4)-violarite ($FeNi_2S_4$)-greigite (Fe_3S_4) have been studied using Mössbauer spectroscopy to show low-spin Fe^{2+} in the octahedral sites (Vaughan and Craig 1985). Ni_3S_4 is metallic and it exhibits itinerant electron ferrimagnetism as a result of strong covalence (Manthiram and Jeong 1999). Certain physical properties of these and other thiospinel minerals including carrollite ($CuCo_2S_4$), linnaeite (Co_3S_4) and siegenite [$(Co, Ni)_3S_4$], which occur in ore deposits and daubreelite [$(Fe,Mn,Fe)Cr_2S_4$], which is present in meteorites, have been interpreted using molecular orbital and band theories (Vaughan et al. 1971).

Only in the last decade has it become clear that, in fine grained marine and terrestrial sediments, greigite is an important carrier of the magnetic information needed by paleomagnetists. In particular, the neoformation of greigite in sediments can complicate or compromise studies of environmental magnetism and geomagnetic field behavior using such rocks (Roberts 1995; Jiang et al. 2001; Roberts and Weaver 2005). Dekkers et al. (2000) provide detailed information on the rock magnetic properties of greigite, and this topic is discussed further below.

PROPERTIES OF SULFIDE NANOPARTICLES

This chapter has been chiefly concerned with the electrical and magnetic properties of bulk sulfide materials. In the past two decades there has been considerable interest in nanoparticles of sulfide-based semiconductors with critical dimensions in the range of 1-20 nm, many of which are "quantum dots." These small particles can be viewed as having properties intermediate between a molecule and a bulk solid. The optical, magnetic, electrical and chemical properties of such nanoparticles are often strongly composition, size, and shape dependant, resulting in novel uses in a range of optical or electronic devices, as well as in catalysts. Two fundamental factors, related to the size of the individual semiconductor nanoparticles, are responsible for their unique properties. The first is the large surface to volume ratio. As the particle becomes smaller, the ratio of the number of surface atoms to those in the interior increases, e.g., in a typical approximately spherical 1nm nanoparticle *ca* 80% of the atoms are at the surface. The surface plays a very significant role in the properties of the nanomaterial. The second factor is the relationship between the electronic properties of the material and the critical dimensions of the particle. In semiconductors, these size dependant properties appear when the radius of the particle is comparable to the excitonic (Bohr) radius of the bulk material. The band gap increases in energy with decreasing particle diameter, as a result of a quantum size effect due to confinement of the electron and hole in a small volume. This phenomenon gives rise to discrete energy levels rather than the continuous band found in the corresponding bulk material (Pickett and O'Brien 2001). This produces a shift in the band gap, and light absorption moves towards the higher energy end of the spectrum accompanied by the appearance of a strong peak, excitonic in origin rather than the band edge associated with a bulk material. The manipulation of particle size, as

well as chemical composition, leads to control over the chemical and physical behavior of the nanoparticles (Kulkarni et al. 2001). The variation of band gap with size can be modeled using the particle in the box model as first described by Brus (1984).

Chalcogenide semiconductor nanomaterials have been studied in detail, especially those of zinc, cadmium, mercury and lead, and there is some work on transition metal sulfides e.g., those of copper and nickel. Potential applications are anticipated in color change materials such as phosphors, and in photovoltaics. The quantum size effects described above have been demonstrated in a study of quantum dot sized particles of CdS with different and well-defined size distributions (Vossmeyer et al. 1994). A shift in the excitonic peak to energies as high as 4.8 eV was observed for nanoparticles with a mean diameter of 0.64 nm, compared to bulk CdS, which has a 2.42 eV band gap (Fig. 29). Substitutional doping of these chalcogenide semiconductor nanomaterials with paramagnetic transition-metal ions can also produce magnetic materials termed dilute magnetic semiconductors (DMS). Figure 30 shows a comparison of the photoluminescence and photoluminescence excitation data for nanoscale and bulk ZnS:Mn. The large shift of 1215.5 nm in the excitation spectrum is attributed to an increase in the value of the *s-p* electron band gap in the ZnS nanocrystal from quantum confinement. Reducing the particle size will also affect the magnetic properties of the phases. For example, α-NiS nanoplates show paramagnetism with weak ferromagnetic interactions, unlike the bulk counterpart which is antiferromagnetic (Zhang et al. 2005a). The possibility of using sulfide-bearing nanoparticles as magnetic devices remains largely unexplored, although the magnetic properties of a range of hybrid materials containing NiS has been assessed by Lui et al (2005).

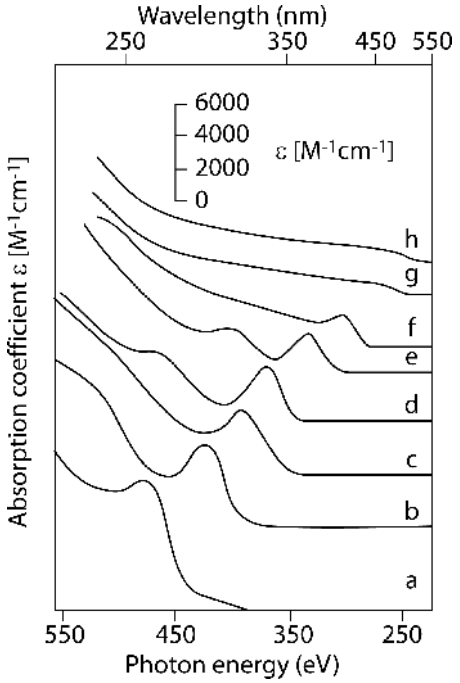

Figure 29. Electronic absorption spectra of CdS nanoparticles with different mean diameters (nm): (a) 0.64, (b) 0.72, (c) 0.8, (d) 0.93, (e) 1.16, (f) 1.94, (g) 2.8 and (h) 4.8. [Redrawn with permission from Vossmeyer et al. Copyright 1994 American Chemical Society.]

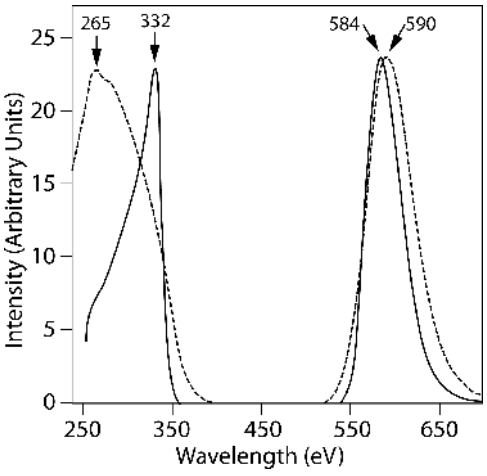

Figure 30. Photoluminescence and photoluminescence excitation spectra of bulk (solid lines) and nanocrystalline (dashed lines) ZnS:Mn. [Used with permission of American Physical Society, from Bhargava et al. (1994), *Physical Review Letters,* Vol. 72, Fig. 1, p. 4162.]

Synthesis of sulfide nanoparticles

Extensive studies have been reported of preparative methods for sulfide nanomaterials, and a range of morphologies including terapodal structures, rods, wires, plates, oblate proloids and spheres are known, as reviewed in Trindade et al. (2001). Fabrication of ordered assemblies of these nanoparticles can be achieved through "top down" processes involving lithography and etching. However, this approach usually only yields semiconductor nanostructures of good structural and optical quality for sizes larger than 50 nm. Below this size, these fabrication processes result in surface damage which has a detrimental effect on the structural quality and makes it difficult to differentiate between intrinsic and extrinsic properties in the study of electronic and magnetic properties as a function of nanoparticle size. There are also a number of "bottom up" fabrication techniques that rely on nucleation and precipitation processes, either in glass matrices including sol-gel methods, or in solution including the trioctyl-phosphine/ trioctylphosphine oxide (TOP/TOPO) solvent system (Brieler et al. 2005; Trindade et al. 2001). Chemical synthesis of nanoparticles can also be achieved by using a size-limiting "host" such as a surfactant in a nonpolar solvent to form reverse micelles, or the use of microporous substances such as zeolites (Wang and Herron 1987). Several types of nanoparticles synthesized using biomimetric processes have been reported, including bio-inorganic complexes of CdS-ferritin (Wong and Mann 1996; Trindade et al. 2001). In a number of cases, nanoparticles need to be "capped" to inhibit surface reactions, and to avoid agglomeration and Ostwald ripening. An example is the production of CdS from cadmium sulfate and ammonium sulfide, where styrene is used as a capping agent (Boxall and Kelsall 1991).

Complex nanocomposites can be made by successive reactions, for instance reacting relatively soluble HgS nanoparticles with dissolved Cd to form HgS with a CdS coating (Häesselbarth et al. 1993); an early example of a "core-shell" particle. Advances in the development of sulfide-polymer nanocomposites for optical, magnetic, and electronic uses is driven by new fabrication methods which are devised to produce emitting diodes, photodiodes, solar cells and gas sensors (Godovsky 2000). These often comprise conductive polymer matrices containing embedded semiconducting nanoparticles of sulfides such as ZnS, CdS, PbS or CuS. Light emitting diodes and lasers exploit the electroluminescence properties of nanocomposites that result from the radiative recombination of holes in the valence band and electrons in the conduction band (Godovsky 2000). A very efficient electroluminescent nanocomposite comprises relatively high band gap CdS surrounding a lower band gap CdSe core (with a semi-conducting polymer and a dodeylamine capping agent). Nanocomposite devices are much more efficient than those employing only CdSe, exhibiting enhanced properties such as low operating voltages and voltage dependent color emission (Schlamp et al. 1997).

It is not possible to provide comprehensive coverage of the sulfide nanoparticle literature in this chapter due to the vast amount of information available. The pertinent concepts will, therefore, be covered in a case study of ZnS in both pure and doped form.

Case study: pure and transition metal (*TM*) ion doped ZnS

ZnS is a wide band gap II-IV semiconductor and is a good host material as a result of its band gap characteristics (~3.6 eV). *TM* ion doping in ZnS nanocrystals (ZnS:*TM*) enhances the optical transition efficiency of the charge carriers (electrons or holes) and increases the number of optically active sites (Karar et al. 2004). ZnS:*TM* may also exhibit ferromagnetism, allowing the potential for bifunctional devices with luminescent and magnetic properties. Manganese is one of the most common *TM* dopants because: (1) it can be incorporated into a (II, IV) semiconductor host in large proportions without altering the crystal structure; (2) it has a relatively large magnetic moment and (3) it is electrically neutral in a (II, IV) host, thus avoiding the formation of any acceptor or donor impurities in the crystal (Bandaranayake et al. 1997). Manganese usually substitutes in the Zn-lattice sites as a divalent ion with a tetrahedral

crystal field (Brieler et al. 2005). Figure 31 shows a TEM micrograph of doped chalcogenide semiconductor nanoparticles. The excitation and decay of the Mn^{2+} ion produces an intense yellow luminescence at ~585 nm as a result of the electronic interaction between the Mn^{2+} ions *d*-electron states and the *s-p* electronic states of the host ZnS nanostructure (Bhargava et al. 1994). The incorporation of *TM* ions into the ZnS nanostructures is revealed in the photoluminescence spectra (Singh et al. 2004). The luminescence of ZnS at 425 nm is affected by *TM* dopants in terms of the decay time and the intensity (Kulkarni et al. 2001). Yuan et al. (2004) found that the intensity of the ZnS-related emission decreased with increasing Mn concentrations, while the Mn^{2+} emission intensity increased with an increasing concentration of Mn^{2+} incorporated in the nanostructure at lower Mn concentrations. However, the decrease in Mn^{2+} emission at higher Mn contents was possibly due to the presence of Mn^{3+} or Mn^{4+} ions, which act as efficient quenchers of the emission due to the low position of the charge transfer absorption band of these ions in the sulfide. Figure 32 shows a schematic diagram of the complex optical processes observed in wide gap (II, Mn) VI semiconductors. The magnetic properties of the ZnS:Mn system also provide information about the relationship between the *s-p* electron hole of the host (ZnS) and the *d*-electrons of the impurity (Mn). Magnetization is often found to be higher in ZnS:Mn nanostructures as compared with their bulk counterparts (Yuan et al. 2004). Schuler et al. (2005) used X-ray emission and absorption spectroscopy to examine the electronic structure of $Zn_{1-x}Mn_xS$ and found that these compounds exhibit similar behavior to that of MnS within 4 eV of the Fermi energy, with the Zn *s* and *p* states providing little influence on the Mn 3*d* bonding states. A band gap of 3 eV (±1.0 eV) was found.

TM doped ZnS nanoparticles can be synthesized using various methods such as solid-state reaction, sol-gel processes and hydrothermal techniques (Table 4). The first synthesis of nanoscale Mn-doped ZnS employed a precipitation reaction and was reported by Bhargava et al (1994). They maintained particle separation with a surfactant, which resulted in an increase in the intensity of the yellow Mn^{2+} emission as a result of surface passivation of the ZnS:Mn particles. Nanoscale TM doped ZnS is used commercially as a phosphor and in electroluminescent devices such as electronic displays (Trindade et al. 2001). Correct treatment of the doped ZnS nanoparticle surface also allows for selective attachment to specific bacterial cell walls for

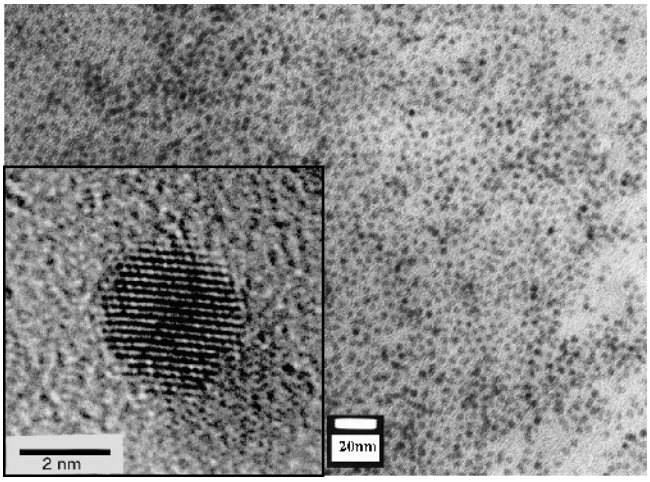

Figure 31. Transition electron micrograph and High Resolution-transition electron microbgraph showing doped chalcogenide semiconductor nanoparticles. The lattice fringes in the HRTEM micrograph are indicative of the crystalline nature of the particles. [Reproduced with kind permission of Paul O'Brien.]

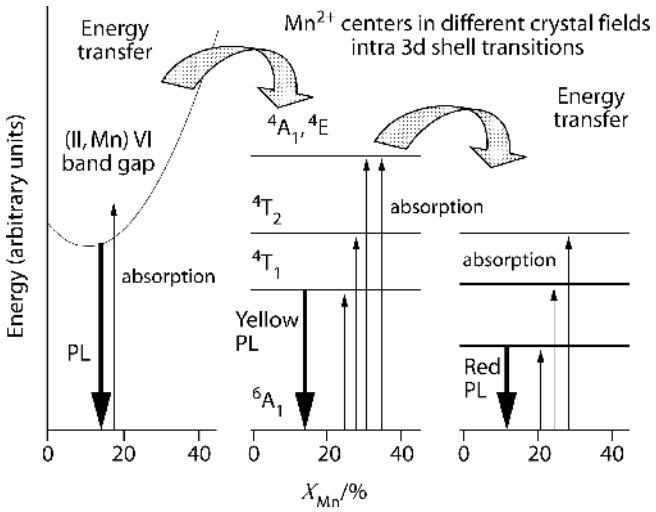

Figure 32. Schematic diagram of the optical processes observed in wide-gap (II,Mn)VI semiconductor nanoparticles (Brieler et al. 2005).

Table 4. Routes for the preparation of ZnS and ZnS:Mn nanoparticles.

Synthetic Method	**Particle Size Range (nm)**	**References**
Solutions of polymeric aducts of zinc alkyls + H_2S	2-4	Li et al. 1994
Arrested precipitation in aqueous and methanolic solutions	<2	Rossetti et al. 1985
Photodegradation of 3 nm particles or precipitation in phosphate containing solution	1.7	Weller et al. 1984
Treatment of zinc containing copolymers with H_2S	<3	Sankaran et al. 1993
Thermolysis of single molecule precursors in TOPO	3.5-4.2	Ludolph and Malik 1998
Precipitation by reacting diethylzinc with hydrogen sulfide in toluene with addition of diethylmanganese in a tetrahydrofuran solvent. Coated with methacrylic acid.	3.5-7.5	Bhargava et al. 1994
Chemical Bath Deposition at 85ºC - ammonium hydroxide and hydrazine with aqueous $ZnSO_4$ thiourea.	4	Singh et al. 2004
Addition of sodium sulfide solution to $Zn(CH_3COO)_2$ and $Mn(CH_3COO)_2$ solutions in iso-propanol medium with polyvinylpyroledone to control the particle size	2-4	Karar et al. 2004
Precipitation with $ZN(CH_3COO)_2$ and NaS - Reaction performed under microwave irradiation.	5	Yang et al. 2005
Metal nanocluster-catalyzed chemical vapor deposition for nanowire growth	20	Radovanovic et al. 2005
NaS added to aqueous solution containing $Zn(CH_3COO)_2$ and $Mn(CH_3COO)_2$with sodium polyphosphate as stabilizing agent.	60-80	Warad et al. 2005

biological labeling (Warad et al. 2005). These sulfide-based diluted magnetic semiconductors also have potential application in the novel area of spin-transport electronics (or spintronics), in which the spin of charge carriers (electrons or holes) is exploited to provide new functionality for microelectric devices (Pearton et al. 2003). However, the ability to tailor their magnetic and electronic properties will be required in much the same way that band gaps are engineered in conventional semiconductors. Research in this area is extensive and ongoing but, as yet, no systematic understanding of the relationship between properties, such as Curie temperature and band gap, exists for these novel magnetic semiconductors (Erwin and Žutic 2004). The synthesis and properties of TM doped ZnS have been recently reviewed by Hu and Zhang (2006).

Sulfide nanoparticles in the environment

Sulfide nanoparticles can be formed in natural aqueous environments due to the gross insolubility of many sulfides in aqueous media (e.g., CdS has a K_{sp} value of ca. 10^{-28}). ZnS typically forms 2-3 nm diameter particles in natural systems as it is fairly insoluble with a low barrier for nucleation (Gilbert and Banfield 2005). CuS nanoparticles, with reported radii of 3-26 nm, have also been reported in oxic waters where they account for substantial fractions of filterable Cu and reduced sulfur (Rozan et al. 2000; Cigleneèki et al. 2005). Transition metal sulfide minerals are often formed as products of the metabolism of sulfate-reducing bacteria in anoxic environments (Posfai and Dunin-Borkowski 2006, this volume). These bacteria can couple the oxidation of carbon to the reduction of aqueous sulfate ions to produce HS^-, which in the presence of a suitable counter-ion, will precipitate as a metal sulfide. Labrenz et al. (2000) have shown that the first sulfide mineral formed by bacteria in groundwater associated with an abandoned Pb-Zn ore deposit is ZnS, with 3-5 nm particles formed in proximity to the bacteria. However, biogenic sulfide nanoparticles can also include mackinawite, pyrite, marcasite, greigite and pyrrhotite, with the product being dependant on solution chemistry (Benning et al. 2000). Microbial sulfide production rates reported by Sahm et al. (1999) correspond to production of fraction of a milligram quantities of nanocrystalline metal sulfides per cubic centimeter per year, which is significant over geological time scales. For further information on sulfide nanoparticles in the environment, see Banfield and Zhang (2001).

APPLICATIONS

Electronics

One of the major areas of potential technological exploitation of sulfides is as photovoltaics in solar energy conversion devices, using thin films on various substrates in conjunction with various organic polymers (Fuhs and Klenk 1998). In particular, chalcopyrite-like structures/stoichiometries such as $CuInS_2$ (the mineral roquesite), which has an ideal band gap of 1.5 eV, have been investigated. Production of vapor-deposited thin films with efficiencies in excess of 10% make commercial exploitation a genuine possibility and assessment continues (Klenk et al. 2005). CdTe also has a band gap of 1.5 eV and photovoltaic devices with outputs of 50W are commercially available while potential CdTe/CdS heterojunction thin film solar cells have yielded efficiencies of 16.5% on coated glass substrates (Albin et al. 2002).

Nanoparticle fabrication has boosted potential developments, especially when nanoparticles are used in conjunction with polymers or other semiconductors. PbS is a good photovoltaic because it has mobile electrons and holes, the lifetime of excited photoelectrons allows them to be "collected" and, importantly, quantum dot sized PbS nanoparticles (~4 nm) have a wide spectral absorption range (Plass et al. 2002; Watt et al. 2005). Nanocomposites involving oleic acid and octylamine capped PbS in poly[2-methoxy-5-(2′-ethylhexyloxy *p*-phenylenevinylene)] (MEH-PPV) have shown particularly good photovoltaic response with the octylamine-capped PbS showing response in the infrared region (Zhang et al. 2005b).

MoS_2 and WS_2 are two other sulfides that also have potential uses as photovoltaics in solar cells (Jaeger-Waldau et al. 1993; Bernede et al. 1999). A further use of $CuIn_{1-x}Ga_xS_2$ thin films is in water splitting photoelectrochemical cells using a multi-band gap process employing RuO_2 and RuS_2 as photocatalysts (Dhere and Jahagirdar 2005).

Takayama and Takagi (2006) have proposed the use of the magnetic transition in pyrrhotite in phase-change memory devices. They demonstrated the thermally controlled switching of the two magnetic states of pyrrhotite in $Fe_{0.92}S$ ($Fe_{0.74}S_8$) by continual thermal cycling over the ferrimagnetism transition temperature at 580 K. Switching between the ferrimagnetic and the superparamagnetic states takes place with total recovery of the ferrimagnetic state, due to the ordering of the cation vacancies. The authors propose development of pyrrhotite thin films.

Paleomagnetic investigations

Mineral phases which have remanent magnetism are essential for paleomagnetic studies. Although magnetite (including maghemite and titanomagnetite) is the predominant mineral for studying rock magnetism, pyrrhotite and greigite can be the dominant contributors in sediments, and pyrrhotite in magmatic and hydrothermal ore deposits. In clastic sediments, detrital allogenic magnetite predominates whereas sulfides, which are easily broken down during transport, are usually authigenic or syndiagenetic in origin. However, in young sediments where sedimentation rates have been high, pyrrhotite of detrital origin has been recognized (Horng and Roberts 2006). Authigenic Fe-sulfides, such as pyrrhotite and greigite, form in anoxic conditions during diagenesis; this typically involves the bacterial reduction of sulfate to provide a source of H_2S and the release of Fe from detrital iron oxides. As greigite is relatively unstable (Benning and Barnes 1998), and does not survive the oxidation reactions that characterize many geological processes (and often convert it to pyrite), it is only present in younger sedimentary sequences. Pyrrhotite can retain original magnetic signatures over long time spans, but even low oxygen fugacities at 500 °C can cause the conversion of pyrrhotite to magnetite (Bina and Daly 1994) with consequences for the resetting of the rock magnetic signature in metamorphosed rocks. In studies of ore formation, paleomagnetic analysis of ores and host rocks have been employed as a means of age dating mineralization where suitable radiometric minerals are absent; it is particularly useful for low temperature hydrothermal mineralization (Rochette et al. 2001).

The increasing use of greigite in paleomagnetic studies of younger sedimentary rocks relates to the increasing awareness of its presence in these sediments (Horng et al.; Thompson and Cameron 1995). The greigite in these rocks typically forms in early diagenesis so its paleomagnetic information relates closely to the time of deposition and, if the sediment remains unoxidized, it can be used a reliable paleomagnetic indicator. For example, the Pleistocene (Pastorian) estuarine clays of the Norfolk (UK) coast have proved highly ferrimagnetic and X-ray diffraction and scanning electron microscopy revealed 1-2 μm grains of greigite to be the only magnetic phase present (Thompson and Cameron 1995). The greigite was formed by reduction of iron by organic matter during diagenesis in the clays. Natural remanent magnetization measurements made using high sensitivity magnetometers on oriented cores exposed a magnetic polarity reversal during the "blue" clay deposition while oxidation has affected the sulfides in other "brown" clays in the sequence. Greigite is also responsible for stable characteristic remanent magnetism in Neogene sediments in north western New Zealand (Rowan and Roberts 2006). These sediments were characterized by high accumulation rates that restricted concentrations of organic matter and allowed incomplete pyritization to take place and, as a result, authigenic greigite to be preserved. The source of iron was detrital magnetite dissolved by H_2S released by bacteria activity in anoxic conditions. Some of the greigite is thought to have formed >1my after sedimentation, signaling caution when interpreting authigenic sulfides in paleomagnetic studies (Rowan and Roberts 2006). In deltaic sequences, diagenetic greigite is a major contributor to rock magnetism in the clayey lithologies (prodelta, delta front marine

clays, lagoonal clays) while magnetite is dominant in the fluvio-deltaic sands. In oilfield borehole samples of a deltaic succession, greigite–bearing samples have been used to determine stratigraphic correlation and sedimentation rates (Thompson and Cameron 1995).

The recognition that the pyrrhotites, and monoclinic pyrrhotite in particular, can be important contributors to the magnetic properties of rocks has led to a significant number of publications dealing with parameters of interest in geomagnetism and paleomagnetism. Readers are referred to articles by Dekkers (1988, 1989), Menyeh and O'Reilly (1995, 1997) and O'Reilly et al. (2000) as examples of such studies. Magnetic remanence was determined from pyrrhotite-bearing sulfide in core samples from the active 26N° TAG hydrothermal field associated with the North Atlantic mid-oceanic ridge. As the deposits are formed in the last 140 ka, no magnetic reversal was apparent but the data were surprisingly complex, with highly variable inclinations over relatively short distances (Zhao et al. 1998). Multistage mineralization, resetting during repeated hydrothermal episodes (including paragentically late veining), local tectonic activity and the potential effect of magnetic excursions all may have contributed to the small scale complexity. These magnetic excursions have also been recognized in sediments bordering the Atlantic using paleomagnetic studies (Hall et al. 1997) allowing paleomagnetic stratigraphic correlation over long distances.

Pyrrhotite concentrations are common in many ancient sulfide-bearing mineral/ore deposits and have been used to provide paleomagnetic information. In particular paleomagnetic investigations of the low temperature, epigenetic hydrothermal base-metal Mississippi Valley Type (MVT) deposits have been used to help with age dating of the mineralization using the determination of paleopoles during mineralizing episodes. Sphalerite-dominated epigenetic MVT mineralization hosted by Lower Ordovician carbonates at Madison-Jefferson City, Tennessee, contains pyrrhotite (with minor magnetite) that gave characteristic remanent magnetism that indicated a paleopole at 128.7°E, 34.0°N, demonstrating that it acquired its primary chemical remanence at 316 ± 8 Ma. This places the mineralization after the peak orogenesis (Alleghanian) and the tectonic context suggests that formation is consistent with models of topographically or thrust-driven driven fluid flow. Paleomagnetic analysis of host rocks and mineralization in Tri-State MVT district show that the remanence of the samples is carried mostly by single to pseudosingle domain pyrrhotite and/or magnetite. The mineralization in the boulders yields a characteristic remanent magnetism with an inclination of 7.4° ± 1.9°, which constrains ore genesis to an equatorial paleolatitude, which for the Tri-State area has only been true in the Middle Pennsylvanian to the Middle Triassic. Two genetic models for ore deposition are constrained by the paleomagnetic data that support a single major epigenetic MVT ore-forming event during either the Late Pennsylvanian (304 ± 6 Ma) or the Late Permian (257 ± 10 Ma) (Symons and Stratakos 2002). Paleomagnetic analysis of sulfide ore components, dolomitic carbonate host rocks, altered igneous rocks and later mineralization established an Early Permian age of ~272 ± 18 Ma origin for the Sherman-type deposits of the Colorado mineral belt, supporting a Mississippi-Valley type origin for those deposits (Symons et al. 2000).

Beneficiation of sulfide ores

Due to its ferromagnetic properties and its wide occurrence in Ni-Cu-Fe magmatic ores, such as those associated with ultramafic intrusions, pyrrhotite is the most common sulfide that has been magnetically separated during mineral processing (Wells et al. 1997; Yalcin et al. 2000; Hu and Sun 2001). In this type of ore deposit it is often the main sulfide present and is associated and intergrown with the main mineral of economic interest, pentlandite $(Fe,Ni)_9S_8$. Pyrrhotite can be nickeliferous and contain inclusions of platinum group elements but is usually of little economic value. However, its separation prior to smelting of the pentlandite (and chalcopyrite) is of enormous economic and environmental benefit (Wells et al. 1997). The different magnetic properties of monoclinic (ferromagnetic) and hexagonal (antiferromagnetic) forms of pyrrhotite requires different approaches to their separation (Schwarz and Vaughan

1972). In addition to the magmatic ores, the magnetic separation of "waste" pyrrhotite from complex base-metal and oxide ores has been achieved successfully (Hudson 1967; Shoji et al. 1974). Recent mineral processing innovations have focused on new flotation methodologies to separate the pyrrhotite (Wells et al. 1997) as well as a combination of techniques by applying magnetic fields to the flotation froth as it leaves the flotation cells (Yalcin et al. 2000).

Secondary methods of magnetic separation of sulfides are sometimes employed. Partially roasting or microwaving and oxidation of Fe-bearing sulfides ores can lead to the development of magnetic surface species ($Fe_{1-x}S$, Fe_3O_4, γ-Fe_2O_3) that improve magnetic separation efficiency. In this way partially oxidized pyrite can be separated from completely oxidized Fe_2O_3 in iron ores, while maghemite forms on the surface of chalcopyrite such that it can be magnetically separated from other copper and base-metal sulfides (Jirestig and Forssberg 1994; Lovas et al. 2003; Uslu et al. 2003). The thermal oxidation of pyrite in coal to pyrrhotite allows its magnetic separation, and sulfides containing magnetic mineral inclusions (magnetite or pyrrhotite) can be selectively separated (Kim et al. 1985; Weng and Wang 1992).

The relative susceptibilities of the paramagnetic sulfides are often employed on the laboratory scale (by using magnetic fields of differing strengths) to separate and concentrate sulfides (Jirestig and Forssberg 1994). On the industrial scale the relatively high magnetic susceptibility of chalcopyrite in a strong applied field means it can be separated from other less susceptible base-metal sulfides, such as galena, (Kim et al. 1995). Zinc recovery at the Boliden complex, Sweden, has been improved by recovering sphalerite from the galena concentrate using a high gradient magnetic separator (Jirestig and Forssberg 1994).

CONCLUDING COMMENTS

The great diversity of electrical and magnetic properties exhibited by the metal sulfides has long been of interest to mineralogists and been exploited in geophysical exploration and mineral extraction technology. Recent decades have seen an even greater awareness amongst geophysists of the importance of sulfide minerals in geomagnetism and paleomagnetism, and considerable growth in interest from materials scientists in the potential for applications of sulfide thin films or nanoparticles. These areas of research are likely to undergo substantial further development, and mineralogists and geochemists are well place to contribute to their development, as well as benefiting from the insights into natural materials afforded by experiments on synthetic samples and the application of new techniques.

ACKNOWLEDGMENTS

The authors are very grateful for the comments received on the manuscript from Richard Harrison, Gerrit van der Laan and Paul O'Brien. We would also like to thank Richard Hartley for his sterling work on the Figures and Helen Weedon for her assistance.

REFERENCES

Abd Al Halim AM, Fiechter S, Tributsch H (2002) Control of interfacial barriers in *n*-type FeS_2 (pyrite) by electrodepositing metals (Co, Cu) forming isostructural disulfides. Electrochim Acta 47:2615-2623

Abraitis P K, Pattrick RAD, Vaughan DJ (2004) Variations in the compositionsal, textural and electrical properties of natural pyrite: a review. Int J Miner Process 74:41-59

Adachi K, Sato K, Takeda M (1969) Magnetic properties of cobalt and nickel dichalcogenide compounds with pyrite stucture. J Phys Soc Japan 26:631-638

Albin D, Dhere R, Wu X, Gessert T, Romero MJ, Yan Y, Asher S (2002) Perturbation of copper substitutional defect concentrations in CdS/CdTe heterojunctions solar cells devices. Meter Res Soc Spring Meeting, Proc Symp F

Allemand J, Wintenberger M (1970) Propriétés structurales et magnetiques de quelques composes du type stannite. Bull Soc Fr Mineral 93:341-396

Andresen AF, Torbo P (1967) Phase transitions in Fe_xS (x = 0.90 - 1.00) studied by neutron diffraction. Acta Chem Scand 21:2841-2848

Aplesnin SS, Petrakovskii GA, Ryabinkina LI, Abramova GM, Kiselev NI, Romanova OB (2004) Influence of magnetic odering on the resisteivity anisotropy of α–MnS single crystal. Solid State Comm 129:195-197

Aplesnin SS, Ryabinkina LI, Abramova GM, Romanova OB, Vorotynov AM, Velikanov DA, Kiselev NI, Balaev AD (2005) Conductivity, weak ferromagnetism , and charge instability in an α-MnS single crystal. Phys Rev B 71:125204

Austin IG, Goodman CHL, Pengelly A (1956) New semiconductors with the chalcopyrite structure. J Electrochem Soc 103:218-219

Baleshta TM, Dibbs HP (1969) An introduction to the theory, measurement and application of semiconductor transport properties of minerals. Mines Branch Technical Bulletin TB 106, Ottawa, Canada

Baleshta TM, Keys JD (1968) Single electrometer method of measuring transport properties of high-resistivity semiconductors. Am J Phys 36:23-26

Bandaranayake RJ, Lin JY, Jiang HX, Sorensen CM (1997) Synthesis and properties of $Cd_{1-x}Mn_xS$ diluted magnetic semiconductor ultrafine particles. J Magn Magn Mat 169:289-302

Banfield JF, Zhang H (2001) Nanoparticles in the environment. Rev Mineral 44:41-51

Benning LG, Barnes HL (1998) *In situ* determination of the stability of iron monosulfides and kinetics of pyrite formation. Mineral Mag 62A:151-152

Benning LG, Wilkin RT, Barnes HL (2000) Reaction pathways in the Fe-S system below 100 °C. Chem Geol 167:25-51

Benoit R (1952) Sur le paramagnetisme des sulfures de fer. Compt Rend 234:2174

Benoit R (1955) Etude paramagnetique des composés binaires. J Chim Phys 52:119-132

Bernardini GP, Borrini D, Caneschi A, Di Benedetto F, Gatteschi D, Ristori S, Romanelli M (2000) EPR and SQUID magnetometry study of Cu_2FeSnS_4 (stannite) and Cu_2ZnSnS_4 (kesterite). Phys Chem Min 27: 453-461

Bernede JC, Pouzet J, Gourmelon E, Hadouda H (1999) Recent studies on photoconductive thin films of binary compounds. Synth Met 99:45-52

Bertaut EF (1953) Contributions a l'étude des structures lacunaires: la pyrrhotine. Acta Cryst 6:557-561

Bhargava RN, Gallagher D, Hong X, Nurmikko A (1994) Optical properties of manganese-doped nanocrystals of ZnS. Phys Rev Lett 72:416-419

Bina M, Daly L (1994) Mineralogical change and self-reversed magnetizations in pyrrhotite resulting from partial oxidation; geophysical implications. Phys Earth Planet Inter 85:83-99

Birkholz M, Fiechter S, Hartmann A, Tributsch H (1991) Sulfur deficiency in iron pyrite (FeS_{2-x}) and its consequences for band-structure models. Phys Rev B 43:11926

Bither TA, Bouchard RJ, Cloud WH, Donohue PC, Siemons WJ (1968) Transition metal pyrite chalcogenides. High pressure synthesis and correlation of properties. Inorg Chem 7:2208-2220

Bither TA, Prewitt CT, Gillson JL, Bierstedt PG, FLippen RB, Young HS (1966) New transition metal dichalcogenides formed at high pressure. Solid State Comm 4:533

Boxall C, Kelsall GH (1991) Photoelectrophoresis of colloidal semiconductors. 1. The technique and its applications. J Chem Soc Faraday Trans 87:3537-3545

Brieler FJ, Grundmann P, Fröba M, Chen L, Klar PL, Heimbrodt W, von Nidda H-A K, Kurz T, Loidl A (2005) Comparison of the magnetic and optical properties of wide-gap (II,Mn)VI nanostructures confined in mesoporous silica. Eur J Inorg Chem:3597-3611

Brown PJ, Neumann K-U, Simon A, Ueno F, Ziebeck KRA (2005) Magnetization distribution in CoS_2; is it a half metallic ferromagnet? J Phys: Cond Matt 17:1583-1592

Brummage WH, Yarger CR, Lin CL (1964) Effect of the exchange coupling of Mn^{++} ions on the magnetic susceptibilities of ZnS:MnS crystals. Phys Rev 133:765-767

Brun del Re R, Lamarche G, Woolley JC (1992) Magnetic behavior of $CuIn_{1-z}Fe_zS_2$. J Phys: Cond Matt 4: 8221-8232

Brus LE (1984) Electron-electron and electron-hole interactions in small semiconductor crystallites: The size dependence of the lowest excited electronic state. J Chem Phys 80:4403-4409

Butler SR, Bouchard RJ (1971) Single crystal growth of pyrite solid solutions. J Cryst Growth 10:163-169

Chattopadhyay T, Brükel T, Burlet P (1991) Spin correlation in the frustrated aniferromagnet MnS_2 above the Néel temperature. Phys Rev B 44:7394-7402

Chattopadhyay T, Brükel T, Holwein D, Sonntag R (1995) Magnetic diffuse scattering from the frustrated antiferromagnet MnS_2. J Magn Magn Mat 140-144:1759-1760

Chen CT, Idzerda YU, Kao C-C, Tjeng LH, Lin H-J, Meigs G (1995) Recent progress in soft-X-ray magnetic circular dichroism. J China Univ Sci Tech 25:1-10

Cheroff G, Keller SP (1958) Optical transmission and photoconductive and photovoltaic effects in activated and unactivated single crystals of ZnS. Phys Rev 111:98-102
Cigleneèki I, Krznariæ D, Helz GR (2005) Voltammetry of copper sulfide particles and nanoparticles: investigation of the cluster hypothesis. Environ Sci Technol 39:7492-7498
Coey JMD, Brusetti R (1975) Hest capacity of nickel sulfide and its semimetal-metal transition. Phys Rev B 11:671-677
Collins MF, Longworth G, Townsend MG (1981) Magnetic structure of bornite, Cu_5FeS_4. Can J Phys 59:535-539
Corliss L, Elliot N, Hastings J (1956) Magnetic structures of the polymorphic forms of manganous sulfide. Phys Rev 104:924-928
Corry CE (2005) <*http://www.zonge.com/ferro/proper_1.htm*>
Cotton FA, Wilkinson G (1972) Advanced Inorganic Chemistry, Interscience, New York
Dalven R (1969) A review of semiconductor properties of PbTe, PbSe, PbS and PbO. Infrared Phys 9:141-184
Dekkers M (1988) Magnetic properties of natural pyrrhotite Part I: Behavior of initial susceptibility and saturation-magnetization-related rock-magnetic parameters in a grain-size dependent framework. Phys Earth Planet Int 52:376-393
Dekkers M (1989) Magnetic properties of natural pyrrhotites. II. High- and low-temperature behavior of J_{rs} and TRM as function of grain size. Phys Earth Planet Int 57:266-283
Dekkers M, Passier HF, Schoonen MAA (2000) Magnetic properties of hydrothermally synthesized greigite (Fe_3S_4)-II. High- and low-temperature characteristics. Geophys J Int 141:809-819
Deulkar SH, Bhosale CH, Sharon M, Neumann-Spallart M (2003) Preparations of non-stoichiometric (Zn, Fe)S chalcogenides and evaluation of their thermal, optical and electrical properties. J Phys Chem Solids 64: 539-544
Dhere NG, Jahagirdar AH (2005) Photoelectrochemical water splitting for hydrogen production using combination of CIGS2 solar cell and RuO_2 photocatalyst. Thin Solid Films 480-81:462-465
Di Benedetto F, Bernardini GP, Caneschi A, Cipriani C, Danti C, Pardi L, Romanelli M (2002) EPR and magnetic investigations on sulphides and sulphosalts. Eur J Mineral 14:1053-1060
Donnay G, Corliss LM, Donnay JDH, Elliot N, Hastings JM (1958) Symmetry of magnetic structures: magnetic structure of chalcopyrite. Phys Rev 112:1917-1923
Dove MT (2002) An introduction to the use of neutron scattering methods in mineral sciences. Eur J Mineral 14:203-224
Doyle FM, Mirza AH (1996) Electrochemical oxidation of pyrite samples with known compositions and electrical properties. Electrochem Proc 96:203-214
Dzyaloshinsky I (1958) A thermodynamic theory of 'weak' ferromagnetism of antiferromagnetics. J Phys Chem Solids 4:241-255
Ellmer K, Hopfner C (1997) On the stoichiometry of the semiconductor pyrite FeS_2. Phil Mag A 75:1129-1151
Ennaoui A, Tributsch H (1984) Iron sulphide solar cells. Solar Cells 13:197-200
Ericsson T, Amcoff Ö, Nordblad P (1997) Superstructure formation and magnetism of synthetic selenian pyrrhotites of $Fe_7(S_{1-y}Se_y)_8$, y<1 composition. Eur J Mineral 9:1131-1146
Ericsson T, Amcoff Ö, Nordblad P (2004) Vacancy ordering in Fe_7Se_8-Fe_7S_8 solid solution studied by Mössbauer, X-ray and magnetization techniques. Hyperfine Interact 90:515-520
Erwin SC, Žutic I (2004) Tailoring ferrimagnetic chalcopyrites. Nature Mater 3:410-414
Fischer G, Grieg D, Mooser E (1961) Apparatus for the measurement of galvanomagnetic effects in high resistance semiconductors. Rev Sci Instrum 32:842-848
Fleet ME (1970) Refinement of the crystal structure of cubanite and polymorphism of $CuFe_2S_3$. Z Krist 132: 276-287
Fleet ME (2006) Phase equilibria at high temperatures. Rev Mineral Geochem 61:365-419
Fok MV (1963) Forbidden band width and effective charge of ions in the crystal lattice of ZnS. Sov Phys Solid State 5:1085-1088
Frueh AJ (1959) The use of zone theory in problems of sulfide mineralogy. II. The resistivity of chalcopyrite. Am Mineral 44:1010-1019
Fuhs W, Klenk R (1998) Thin-film solar cells - overview. EUR 18656, World Conference on Photovoltaic Solar Energy Conversion 1:381-386
Gibart P, Goldstein L, Brossard L (1976) Non stoichiometry in $FeCr_2S_4$. J Magn Magn Mater 3:109-116
Gilbert B, Banfield JF (2005) Molecular-scale processes involving nanoparticulate minerals in biogeochemical systems. Rev Mineral Geochem 59:109-146
Godovsky DY (2000) Device applications of polymer-nanocomposites. Adv Polym Sci 153:163-205
Grice JD, Ferguson RB (1974) Crystal structure refinement of millerite (β-NiS). Can Mineral 12:248-252
Häesselbarth A, Eychmueller A, Eichberger R, Giersig M, Mews A, Weller H (1993) Chemistry and photophysics of mixed cadmium sulfide/mercury sulfide colloids. J Phys Chem 97:5333-5340

Hall F, Cisowski S, John S (1997) Environmental rock-magnetic evidence of authigenic-magnetic mineral formation/preservation (Amazon Fan). Proc Ocean Drilling Prog: Scientific Results 155:251-270

Harada T (1998) Transport properties of iron dichalcognenides FeX_2 (X = S, Se and Te). J Phys Soc Jap 67: 1352-1358

Haraldsen H (1941a) Über die eisen (II) sulfid Mischkristalle. Z Anorg Chem 246:169-194

Haraldsen H (1941b) Über die hochtemperaturum – wandlungen der eisen (II) sulfid Mischkristalle. Z Anorg Chem 246:195-226

Harrison RJ (2006) Neutron diffraction of magnetic materials. Rev Mineral Geochem 62: in press

Hastings JM, Corliss LM (1976) First-order anitferromagnetic phase transition in MnS_2. Phys Rev B 14:1995-1996

Hastings JM, Elliot N, Corliss LM (1959) Antiferromagnetic structures of MnS_2, $MnSe_2$ and $MnTe_2$. Phys Rev 115:13-17

Hauger R, Kaldis E, von Schulthess G, Wachter P, Zürcher C (1976) Electrical resistivity of Gd and La monochalcogenides as a function of stoichiometry. J Magn Magn Mat 3:103-108

Hirahara E, Murakami M (1958) Magnetic and electrical anisotropies of iron sulfide single crystals. J Phys Chem Solids 7:281-289

Hirone T, Maeda S, Chiba S, Tsuya N (1954) Thermal analysis of iron sulfides at the temperature range of the β-transformation. J Phys Soc Jap 9:500-502

Ho CH, Huang CE, Wu CC (2004) Preparation and characterization of Ni-incorporated FeS_2 single crystals. J Cryst Growth 270:535-541

Hobbs D, Hafner J (1999) Magnetism and magneto-structural effects in transition metal-sulphides. J Phys: Cond Matt 11:8197-8222

Hoffmann V (1993) Mineralogical, magnetic and Mössbauer data of smythite (Fe_9S_{11}). Studia Geophy Geodaet 37:366-381

Holton WC, DeWit M, Watts R K, Estle TL, Schneider J (1969) Paramagnetic copper centres in ZnS. J Phys Chem Solids 30:963-977

Honig JM, Spalek J (1998) Electronic properties of $NiS_{2-x}Se_x$ single crystals: from magnetic Mott-Hubard insulators to normal metals. Chem Mater 10:2910-2929

Horng C-S, Roberts AP (2006) Authigenic or detrital origin of pyrrhotite in sediments?: resolving a paleomagnetic conundrum. Earth Planet Sci Lett 241:750-762

Horng C-S, Torii M, Shea K-S, Kao S-J (1998) Inconsistent magnetic polarities between greigite - and pyrrhotite/magnetite-bearing marine sediments from the Tsailiao-chi section, southwestern Taiwan. Earth Planet Sci Lett 164:467-481

Hu H, Zhang W (2006) Synthesis and properties of transition metals and rare-earth metals doped ZnS nanoparticles. Opti Mater 28:536-550

Hu Z, Sun C (2001) Separating pure minerals from Jinchuan copper-nickel mine. Nonferrous Met 53:73-75

Hudson SB (1967) High-intensity wet magnetic separation of a zinc cleaner tailing from Broken Hill, New South Wales. Ore Dressing Investigations 672:3

Hulliger F (1959) Über den zusammenhang zwischen magnetismus und elektrischer leitfähigkeit von verbindungen mit ubergangselementen. Helv Phys Acta 32:615-654

Hulliger F (1968) Crystal chemistry of the chalcogenides and pnictides of the transition elements. Struct Bonding 4:83-229

Jaeger-Waldau A, Lux-Steiner MC, Bucher E, Jaeger-Waldau G (1993) WS_2 thin films: a new candidate for solar cells. *In:* Conference Record of the IEEE Photovoltaic Specialists Conference. 597-602

Jarrett HS, Cloud WH, Bouchard RJ, Butler SR, Frederick CG, Gillson JL (1968) Evidence for itinerant d-electron ferromagnetism. Phys Rev Lett 21:617-620

Jellinek F (1972) Sulfides, Selenides and Tellurides of the Transition Elements. MTP International Review of Science. Series 1, vol. 5, Butterworth

Jiang JZ, Gerward L, Frost D, Secco R, Peyronneau J, Olsen JS (1999) Grain-size effect on pressure-induced semiconductor-to-metal transition in ZnS. J Appl Phys 88:6608-6610

Jiang W-T, Horng C-S, Roberts AP, Peacor DR (2001) Contradictory magnetic polarities in sediments and variable timing of neoformation of authigenic greigite. Earth Planet Sci Lett 193:1-12

Jirestig JA, Forssberg KSE (1994) Magnetic separation in sulfide processing. Trans Soc Min Metall Exploration 294:176-181

Kamigaichi T (1956) Electrical conductivity and thermoelectric power of FeS_x (pyrrhotite). J Sci Hiroshima Univ Ser A 19:499-505

Karar N, Singh F, Mehta BR (2004) Structure and photoluminescence studies of ZnS:Mn nanoparticles. J Appl Phys 95:656-660

Kautz RL, Dresselhaus MS, Adler D, Linz A (1972) Electrical and optical properties of NiS_2. Phys Rev B 6: 2078-2082

Kawiaminami M, Okazaki A (1970) Neutron diffraction study of Fe_7S_8. II. J Phys Soc Jap 29:649-655

Keys JD, Horwood JL, Baleshta TM, Cabri LJ, Harris DC (1968) Iron-iron interaction in iron-containing zinc sulfide. Can Mineral 9:453-467

Kim YS, Fujita T, Hashimoto S, Shimoiizaka J (1985) The removal of copper sulfide minerals from lead flotation concentrate of black ore by high-gradient magnetic separation. Compt Rend 15:381-390

Klein UF, Wortman G, Kalvius GM (1976) High-pressure Mössbauer study of hyperfine interactions in magnetically ordered europium chalcogenides: EuO, EuS, EuTe. J Magn Magn Mat 3:50-54

Klenk R, Klaer J, Scheer R, Lux-Steiner MC, Luck I, Meyer N, Ruehle U (2005) Solar cells based on $CuInS_2$ - an overview. Thin Solid Films 480-481:509-514

Kobayashi H, Kamimura T, Ohishi Y, Takeshita N, Mori N (2005) Structural and electrical properties of stoichiometric FeS compounds under high pressure at low temperature. Phys Rev B 71:014110

Kravchenko AF, Timchenko A K, Godovikov AA (1966) Electrophysical properties of galena from different deposits. Dokl Akad Nauk SSSR 167:74-77

Krill G, Panissod P, Lapierre MF, Gautier F, Robert C, Nassr Eddine M (1976) Magnetic properties and phase transitions of the metallic CuX_2 dichalcogenides (X = S, Se, Te) with pyrite structure. J Phys C 9:1521-1533

Krupp RE (1994) Phase-transitions and phase-transformations between the low-temperature iron sulfides mackinawite, gregite, and smythite. Eur J Mineral 6:265-578

Kruse O (1990) Mössbauer and X-ray study of the effects of vacancy concentration in synthetic hexagonal pyrrhotites. Am Mineral 75:755-763

Kulkarni S K, Winkler U, Deshmukh N, Borse PH, Fink R, Umbach E (2001) Investigations on chemically capped CdS, ZnS and ZnCdS nanoparticles. App Surf Sci 169-170:438-446

Labrenz M, Druschel G K, Thomsen-Ebert T, Gilbert B, Welch SA, Kemner K, Logan GA, Summons R, De Stasio G, Bond PL, Lai B, Kelly SD, Banfield JF (2000) Natural formation of sphalerite (ZnS) by sulfate-reducing bacteria. Science 290:1744-1747

Larach S, Turkevich J (1955) Magnetic properties of zinc sulfide and cadmium sulfide phosphors. Phys Rev 98: 1015-1019

Letard I, Sainctavit P, Menguy N, Valet J-P, Isambert A, Dekkers M, Gloter A (2005) Mineralogy of greigite Fe_3S_4. Physica Scripta T115:489-491

Li F, Franzen HF (1996) Ordering, incommensuration, and phase transition in pyrrhotite. Part II: a high-temperature X-ray powder diffraction and thermomagnetic study. J Solid State Chem 126:108-120

Li F, Franzen HF, Kramer MJ (1996) Ordering, incommensuration, and phase transition in pyrrhotite. Part I: a TEM study of Fe_7S_8. J Solid State Chem 124:264-271

Li X, Fryer JR, Cole-Hamilton DJ (1994) A new, simple and versitile method for the production of nano-scale particles of semiconductors. Chem Comm:1715-1716

Lin MS, Hacker H (1968) Antiferromagnetic transitions in MnS_2 and $MnTe_2$. Solid State Comm 6:687-689

Liu W-J, He W-D, Wang Y-M, Wang D, Zhang Z-C (2005) New approach to hybrid materials: functional sub-micrometer core/shell particles coated with NiS clusters by γ-irradiation. Polymer 46:8366-8372

Lotgering FK (1956) Ferrimagnetism of sulfides and oxides. Philips Res Rep 11:190-217, 213-249, 337-350

Lovas M, Murova I, Mockovciakova A, Rowson N, Jakabsky S (2003) Intensification of magnetic separation and leaching of Cu ores by microwave radiation. Separat Purif Tech 31:291-299

Ludolph B, Malik MA (1998) Novel single molecule precursor routes for the direct synthesis of highly monodispersed quantum dots of cadmium or zinc sulfide or selenide. Chem Comm 17:1849-1850

Makovicky E (2006) Crystal structures of sulfides and other chalcogenides. Rev Mineral Geochem 61:7-125

Manthiram A, Jeong YU (1999) Ambient temperature synthesis of spinel Ni_3S_4: an itinerant electron ferrimagnet. J Solid State Chem 147:679-681

Marusak LA, Mulay LN (1979) Mössbauer and magnetic study of the antiferro to ferrimagnetic phase transition in Fe_9S_{10} and the magnetokinetics of the diffusion of iron atoms during the transition. J Appl Phys 50: 1865-1867

Marusak LA, Mulay LN (1980) Polytypism in the cation-deficient iron sulfide, Fe_9S_{10}, and the magnetokinetics of the diffusion process at temperatures about the antiferro- to ferrimegnetic (λ) phase transition. Phys Rev B 21:238

McCammon CA, Price DC (1982) A Mössbauer effect investigation of the magnetic behavior of (iron, cobalt) $sulfide_{1+x}$ solid solutions. J Phys Chem Solids 43:431-437

McElhinny MW (1973) Paleaomagnetism and Plate Tectonics, Cambridge University Press

Menyeh A, O'Reilly W (1995) The coercive force of fine particles of monoclinic pyrrhotite (Fe_7S_8) studied at elevated temperature. Phys Earth Planet Int 89:51-62

Menyeh A, O'Reilly W (1997) Magnetic hysteresis properties of fine particles of monoclinic pyrrhotite Fe_7S_8. J Geomag Geoelec 49:965-976

Morehead FF (1963) A Dember effect study of shifts in the stoichiometry of ZnS. J Electrochem Soc 110:285-288

Morehead FF, Fowler AB (1962) The Dember effect in ZnS-type materials. J Electrochem Soc 109:688-695

Murakami M, Hirahara E (1958) A certain anomalous behavior of iron sulfides. J Phys Soc Jap 13:1407
Muro T, Shishidou T, Oda F, Fukawa T, Yamada H, Kimura A, Imada S, Suga S, Park SY (1996) Magnetic circular dichroism of the S 2p, Co 2p, and Co 3p core absorption and orbital angular momentum of the Co 3d state in low-spin CoS_2. Phys Rev B 53:7055-7058
Nave R (2000) SQUID Magnetometer, HyperPhysics *<http://hyperphysics.phy-astr.gsu.edu/Hbase/hframe.html>*
Néel L (1953) Some new results on antiferromagnetism and ferromagnetism. Rev Mod Phys 25:58-63
Néel L, Benoit R (1953) Magnetic properties of certain disulfides. Compt Rend 237:444-447
Nikolic PM, Uric S, Todorovic DM, Blagojevic V, Urosevic D, Mihajlovic P, Bojicic AI, Radulovic KT, Vasiljevic-Radovic DG, Elazar J, Dimitrijevic M (1999) Some thermal and electronic transport properties of mineral marmatite (ZnS:Fe). Mat Res Bull 34:2247-2261
Nimtz G, Schlicht B (1983) Narrow-Gap Semiconductors, Springer-Verlag, Berlin
Novakova AA, Gendler TS (1995) Metastable structural-magnetic transformations in sulfides in course of oxidation. J Radioanal Nucl Chem 190:363-368
O'Connor CJ (1982) Magnetochemistry - Advances in theory and experimentation. Prog Inorg Chem 29:203
Ohsawa A, Yamaguchi Y, Watanabe H, Itoh H (1976a) Polarized neutron diffraction study of cobalt disulfide. II. Covalent magnetic moment around the sulfur atoms. J Phys Soc Jap 40:992-995
Ohsawa A, Yamaguchi Y, Watanabe H, Itoh H (1976b) Polarized neutron diffraction study of cobalt disulfide. I. Magnetic moment distribution of cobalt disulfide. J Phys Soc Jap 40:986-991
O'Reilly A, Hoffman V, Chouker AC, Soffel HC, Manyeh A (2000) Magnetic properties of synthetic analogues of pyrrhotite ore in the grain size range 1-24 μm. Geophys J Int 142:669-683
Panissod P, Krill G, Lahrichi M, Lapierre-Ravet MF (1979) Magnetic properties of the $CoS_{2-x}Se_x$ compounds II. Neutron diffraction and NMR investigation of the magnetism and the 'metamagnetic' transition. J Phys C 12:4281-4294
Parasnis DS (1956) The electrical resistivity of some sulfide and oxide minerals and their ores. Geophys Pros 4:249-278
Pattrick RAD, van der Laan G, Henderson CMB, Kuiper P, Dudzik E, Vaughan DJ (2002) Cation site occupancy in spinel ferrites studied by X-ray magnetic circular dichroism: developing a method for mineralogists. Eur J Mineral 14:1095-1102
Pearce CI, Coker VS, van der Laan G, Pattrick RAD (2006a) Magnetic properties of ferrimagnetic sulfides as defined by X-ray magnetic circular dichroism: troilite (FeS) to pyrrhotie (Fe_7S_8). (in preparation)
Pearce CI, Henderson CMB, Pattrick RAD, van der Laan G, Vaughan DJ (2006b) Direct determination of cation site occupancies in natural ferrite spinels by $L_{2,3}$ X-ray absorption spectroscopy and X-ray magnetic circular dichroism. Am Mineral 91:880-893
Pearton SJ, Abernathy CR, Overberg ME, Thaler GT, Norton DP, Theodoropoulou N, Hebard AF, Park YD, Ren F, Kim J, Boatner LA (2003) Wide band gap ferromagnetic semiconductors and oxides. J Appl Phys 93:1-13
Perthel R (1960) Über den Ferrimagnetismus nichtstöchiometrischer Eisensulfide. Ann Physik 7:273-295
Petrakovskii GA, Loseva GV, Ryabinkina LI, Aplesnin SS (1995) Metal-insulator transitions and magnetic properties in disordered systems of solid solutions $Me_xMn_{1-x}S$. J Magn Magn Mat 140-144:147-148
Pickett NL, O'Brien P (2001) Syntheses of semiconductor nanoparticles using single-molecular precursors. Chem Rec 1:467-479
Plass R, Pelet S, Krueger J, Graetzel M, Bach U (2002) Quantum dot sensitization of organic-inorganic hybrid solar cells. J Phys Chem B 106:7578-7580
Pósfai M, Dunin-Borkowski RE (2006) Sulfides in biosystems. Rev Mineral Geochem 61:679-714
Powell AV, Vaqueiro P, Knight KS, Chapon LC, Sánchez RD (2004) Structure and magnetism in synthetic pyrrhotite Fe_7S_8: A powder neutron-diffraction study. Phys Rev B 70:014415
Pridmore DF, Shuey RT (1976) The electrical resistivity of galena, pyrite and chalcopyrite. Am Mineral 61: 248-259
Radovanovic PV, Barrelet CJ, Gradeèak S, Quian F, Lieber CM (2005) General synthesis of manganese-doped II-VI and III-V semiconductor nanowires. Nano Lett 5:1407-1411
Rajamani V, Prewitt CT (1974) The crystal structure of millerite. Can Mineral 12:253-257
Ramesha K, Seshadri R, Ederer C, He T, Subramanian MA (2004) Experimental and computational investigation of structure and magnetism in pyrite $Co_{1-x}Fe_xS_2$: Chemical bonding and half-metallicity. Phys Rev B 70: 214409
Rickard D, Luther GW III (2006) Metal sulfide complexes and clusters. Rev Mineral Geochem 61:421-504
Roberts AP (1995) Magnetic properties of sedimentary greigite (Fe_3S_4). Earth Planet Sci Lett 134:227-236
Roberts AP, Weaver R (2005) Multiple mechanisms of remagnetization involving sedimentary greigite. Earth Planet Sci Lett 231:263-277
Rochette P, Lorand J-P, Fillion G, Sautter V (2001) Pyrrhotite and the remanent magnetization of SNC meteorites: a changing perspective on Martian magnetism. Earth Planet Sci Lett 190:1-12

Rodríguez-Carvajal J (1993) Recent advances in magnetic structure determination by neutron powder diffraction. Physica B 192:55-69

Rooymans CJM (1963) A phase transformation in the wurtzite and zinc blende lattice under pressure. J Inorg Nucl Chem 25:253-255

Rossetti R, Hull R, Gibson JM, Brus LE (1985) Excited electronic states and optical spectra of ZnS and CdS crystallites in the 15 to 50 Å size range: Evolution from molecular to bulk semiconducting properties. J Chem Phys 82:552-559

Rowan CJ, Roberts AP (2006) Magnetite dissolution, diachronous greigite formation, and secondary magnetizations from pyrite oxidation: unravelling complex magnetizations in Neogene marine sediments from New Zealand. Earth Planet Sci Lett 241:119-137

Rozan TF, Lassman ME, Ridge DP, Luther GW, III (2000) Evidence for iron, copper and zinc complexation as multinuclear sulphide clusters in oxic rivers. Nature 406:879-882

Sahm K, MacGregor BJ, Jorgensen BB, Stahl DA (1999) Sulphate reduction and vertical distribution of sulphate-reducing bacteria quantified by rRNA slot-blot hybridization in a coastal marine sediment. Environ Microbiol 1:65-74

Samara GA, Drickamer HG (1962) Pressure induced phase transitions in II-VI compounds. J Phys Chem 23: 457-461

Sankaran V, Yue J, Cohen RE, Schrock RR, Silbey RJ (1993) Synthesis of zinc sulfide clusters and zinc particles within microphase-separated domains of organometallic block copolymers. Chem Mater 5:1133-1142

Schieck R, Hartmann A, Fiechter S, Konenkamp R, Wetzel H (1990) Electrical properties of natural and synthetic pyrite (FeS_2) crystals. J Mater Res 5:1567-1572

Schlamp MC, Peng X, Alivisatos AP (1997) Improved efficiencies in light emitting diodes made with CdSe(CdS) core/shell type nanocrystals and a semiconducting polymer. J Appl Phys 82:5837-5842

Schuler TM, Stern A, NcNorton R, Willoughby SD, Maclaren JM, Ederer DL, Perez-Dieste V, Himpsel FJ, Lopez-Rivera SA, Callcott TA (2005) Electronic structure of the dilute magnetic semiconductor $Zn_{0.90}Mn_{0.10}S$ obtained by soft X-ray spectroscopy and first principles calculations. Phys Rev B 72: 045211

Schull C, Wollan E (1956) Applications of neutron diffraction to solid state problems. Solid State Phys 2:137-217

Schutz G, Fischer P, Attenkofer K, Ahlers D (1997) X-ray magnetic circular dichroism. *In:* Roentgen Centennial. Haase A, Landwehr G, Umbach E (eds) p. 341-363

Schwarz EJ, Vaughan DJ (1972) Magnetic phase relations of pyrrhotite. J Geomag Geoelec 24:441-458

Shoji K, Takamura Y, Kuroda A, Shimoiizaka J (1974) Mineral processing of low-grade bismuth-tungsten ore at Akagane mine, Japan. *In:* Proc Int Miner Process Congr. London. Jones M (ed) p. 667-679

Shuey RT (1975) Semiconducting Ore Minerals. Elsevier Scientific Publishing Company

Singh SP, Perales-Perez OJ, Tomar MS, Mata OV (2004) Synthesis and characterization of nanostructured Mn-doped ZnS thin films and nanoparticles. Phys Stat Solidi C 1:811-814

Sleight AW, Gillson JL (1973) Electrical resistivity of cubanite: $CuFe_2S_3$. J Solid State Chem 8:29-30

Snowball IF, Torii M (1999) Incidence and significance of ferrimagnetic iron sulphides in Quaternary studies. *In:* Quaternary Climates and Magnetism. Maher BA, Thompson R (eds) Cambridge University Press, p. 199-230

Sparks JT, Komoto T (1968) Metal to semiconductor transition in hexagonal nickel sulfide. Rev Mod Phys 40: 752-754

Spokes EM, Mitchell DR (1958) Relation of magnetic susceptibility to mineral composition. Min Eng 60: 373-379

Stöhr J (1995) X-ray magnetic circular dichroism spectroscopy of transition metal thin films. J Elect Spect Relat Phenom 75:253-272

Symons DTA, Lewchuk MT, Taylor CD, Harris MJ (2000) Age of the Sherman-type Zn-Pb-Ag deposits, Mosquito Range, Colorado. Econ Geol 95:1489-1504

Symons DTA, Stratakos KK (2002) Paleomagnetic dating of Alleghanian orogenesis and mineralization in the Mascot-Jefferson City zinc district of East Tennessee, USA. Tectonophys 348:51-72

Takayama T, Takagi H (2006) Phase-change magnetic memory effect in cation-deficient iron sulfide $Fe_{1-x}S$. Appl Phys Lett 88:012512

Takeno S, Masumoto K, Kasamatsu Y, Kamigaichi T (1972) Electrical and magnetic properties of cubanite. J Sci Hiroshima Univer Ser C 7:11-19

Tappero R, Lichanot A (1998) A comparative study of the electronic structure of α-MnS (alabandite) calculated by the Hartree-Fock and Density Functional levels of theory. Chem Phys 236:97-105

Tappero R, Wolfers P, Lichanot A (2001) Electronic, magnetic structures and neutron diffraction in B_1 and B_2 phases of MnS: a density functional approach. Chem Phys Lett 335:449-457

Teranishi T (1961) Magnetic and electrical properties of chalcopyrite. J Phys Soc Jap 16:1881-1887

Teranishi T, Sato K, Kondon K (1974) Optical properties of a magnetic semiconductor: chalcopyrite $CuFeS_2$. I. Absorption spectra of $CuFeS_2$ and Fe-doped $CuAlS_2$ and $CuGaS_2$. J Phys Soc Jap 36:1618-1624
Theodossiou A (1965) Measurement of the Hall effect and resistivity in pyrrhotite. Phys Rev 137:1321-1326
Thole BT, Carra P, Sette PF, van der Laan G (1992) X-ray circular dichroism as a probe of orbital magnetization. Phys Rev Lett 68:1943-1946
Thole BT, van der Laan G (1988) Linear relation between X-ray absorption branching ratio and valence-band spin-orbit expectation value. Phys Rev A 39:1943-1947
Thole BT, van der Laan G, Sawatzky GA (1985) Strong magnetic dichroism predicted in the $M_{4,5}$ X-ray absorption spectra of magnetic rare earth materials. Phys Rev Lett 55:2086-2088
Thompson R, Cameron TDJ (1995) Palaeomagnetic study of Cenozoic sediments in North Sea boreholes: an example of a magnetostratigraphic conundrum in a hydrocarbon-producing area. Geol Soc Sp Pub 98: 223-236
Tossell JA (1978) Theoretical studies of the electronic structure of copper in tetrahedral and triangular coordination with sulfur. Phys Chem Min 2:225-236
Townsend MG, Gosselin JR, Tremblay RJ, Webster AH (1976) Semiconductor to metal transition in iron(2+) sulfide. J de Physique, Colloque 4:11-16
Townsend MG, Horwood JL, Hall SR, Cabri LJ (1971a) Mössbauer, magnetic susceptibility and crystallographic investigations of $Cu_4Fe_4S_8$, $Cu_{18}Fe_{16}S_{32}$ and $Cu_9Fe_9S_{16}$. AIP Magnetic Materials Conf Proc 5:887-991
Townsend MG, Tremblay RJ, Horwood JL, Ripley J (1971b) Metal-semiconductor transition in single crystal hexagonal nickel sulfide. J Phys C 4:598-606
Trindade T, O'Brien P, Pickett NL (2001) Nanocrystalline semiconductors: synthesis, properties, and perspectives. Chem Mater 13:3843-3858
Ueda H, Nohara M, Kitazawa K, Takagi H, Fujimori A, Mizokawa T, Yagi T (2002) Copper pyrites CuS_2 and $CuSe_2$ as anion conductors. Phys Rev B 65:155104
Uslu T, Atalay U, Arol AL (2003) Effect of microwave heating on magnetic separation of pyrite. Colloids Surf A 225:161-167
van den Berg CB, van Delden JE, Bouman J (1969) α-transition in FeS- a ferroelectric transition. Phys Status Solidi 36:K89-K93
van der Laan G, Kirkman IW (1992) The 2p absorption spectra of 3d transition metal compounds in tetrahedral and octahedral symmetry. J Phys: Condens Matter 4:4189-4204
van der Laan G, Thole BT (1988) Local probe for spin-orbit interaction. Phys Rev Lett 60
van der Laan G, Thole BT (1991) Strong magnetic X-ray dichroism in 2p absorption spectra of 3d transition metal ions. Phys Rev B 43:13401-13411
van der Laan G, Thole BT, Sawatzky GA, Goedkoop JB, Fuggle JC, Esteva JM, Karnatak RC, Remeika JP, Dabkowska HA (1986) Experimental proof of magnetic X-ray dichroism. Phys Rev B 34:6529-6531
van der Pauw LJ (1958) A method of measuring specific resistivity and Hall effect of discs of arbitrary shape. Philips Res Rep 13:1-9
Vaughan DJ, Burns RG, Burns VM (1971) Geochemistry and bonding of thiospinel minerals. Geochim Cosmochim Acta 35:365-381
Vaughan DJ, Craig JR (1978) Mineral Chemistry of Metal Sulfides, Cambridge Universtiy Press, London
Vaughan DJ, Craig JR (1985) The crystal chemistry of iron-nickel thiospinels. Am Mineral 70:1036-1043
Vaughan DJ, Rosso KM (2006) Chemical bonding in sulfide minerals. Rev Mineral Geochem 61:231-264
Vossmeyer T, Katsikas L, Giersig M, Popovic G, Diesner K, Chemseddine A, Eychmüller A, Weller H (1994) CdS nanoclusters: synthesis, characterization, size dependant oscillator strength, temperature shift of the excitonic transition energy, and reversible absorbance shift. J Phys Chem 98:7665-7673
Wang Y, Herron N (1987) Chemical effects on the optical properties of semiconductor particles. J Phys Chem 91:5005-5008
Warad HC, Ghosh SC, Hematanon B, Thanachayanout C, Dutta J (2005) Luminescent nanoparticles of Mn doped ZnS passivated with sodium hexametaphosphate. Sci Technol Ad Mat 6:296-301
Ward JC (1970) The structure and properties of some iron sulfides. Rev Pure Appl Chem 20:175-206
Watt A, Eichmann T, Rubinsztein-Dunlop H, Meredith P (2005) Carrier transport in PbS nanocrystal conducting polymer composites. Appl Phys Lett 87:253109
Weller H, Koch U, Gutierrez M, Henglein A (1984) Photochemistry of colloidal metal sulfides. 7. Absorption and fluorescence of extremely small ZnS particles. Ber Bunsen-Ges Pys Chem 88:649
Wells PF, Kelebek S, Burrows MJ, Suarez DF (1997) Pyrrhotite rejection at Falconbridge's Strathcona Mill Falconbridge Ltd., Onaping, Ontario, Canada. *In:* Proceedings of the UBC-McGill Bi-Annual International Symposium on Fundamentals of Mineral Processing. Ontario. Finch J, Rao S, Holubec I, (eds) p. 51-62
Weng S, Wang J (1992) Mössbauer spectroscopy study of enhanced magnetic separation of pyrite from coal by microwave irradiation. J Fuel Chem Tech 20:368-374
Willeke G, Blenk O, Kloc C, Bucher E (1992) Preparation and electrical transport properties of pyrite (FeS_2) crystals. J Alloys Comp 178:181-191

Wincott PL, Vaughan DJ (2006) Spectroscopic studies of sulfides. Rev Mineral Geochem 61:181-229
Wong KKW, Mann S (1996) Biomimetic synthesis of cadmium sulfide-ferritin nanocomposites. Adv Mater 8: 928-932
Yalcin T, Sabau A, Wells P (2000) Magnetoflotation of nickel ore. CIM Bulletin 93:97-102
Yamada H, Terao K, Aoki M (1998) Electronic structure and magnetic properties of CoS_2. J Magn Magn Mat 177-181:607-608
Yang H, Huang C, Su X, Tang A (2005) Microwave-assisted synthesis and luminescent properties of pure and doped ZnS nanoparticles. J Alloys Comp 402:274-277
Youn SJ, Min BI, Freeman AJ (2004) Crossroads electronic structure of MnS, MnSe, and MnTe. Phys Stat Solidi B 241:1411-1414
Yuan HJ, Yan XQ, Zhang ZX, Liu DF, Zhou ZP, Cao L, Wang JX, Gao Y, Song L, Liu LF, Zhao XW, Dou XY, Zhou WY, Xie SS (2004) Synthesis, optical and magnetic properties of $Zn_{1-x}Mn_xS$ nanowires grown by thermal evaporation. J Cryst Growth 271:403-408
Zemel JN, Jensen JD, Schoolar RB (1965) Electrical and optical properties of epitaxial films of PbS, PbSe, PbTe, and SnTe. Phys Rev A 140:330-342
Zhang HT, Wu G, Chen XH (2005a) Synthesis and magnetic properties of NiS_{1+X} nanocrystallites. Mat Lett 59: 3728-3731
Zhang S, Cyr PW, McDonald SA, Konstantatos G, Sargent EH (2005b) Enhanced infrared photovoltaic efficiency in PbS nanocrystal/semiconducting polymer composites. 600-fold increase in maximum power output via control of the ligand barrier. Appl Phys Lett 87:233101
Zhao X, Housen B, Solheid P, Xu W (1998) Magnetic properties of leg 158 cores: the origin of remanence and its relation to alteration and mineralization of the active TAG mound. Proc Ocean Drilling Prog: Scientific Results 158:337-351